



CERN-EP-2017-320
 LHCb-PAPER-2017-048
 22 December 2017

First measurement of the *CP*-violating phase $\phi_s^{d\bar{d}}$ in $B_s^0 \rightarrow (K^+ \pi^-)(K^- \pi^+)$ decays

The LHCb collaboration[†]

Abstract

A flavour-tagged decay-time-dependent amplitude analysis of $B_s^0 \rightarrow (K^+ \pi^-)(K^- \pi^+)$ decays is presented in the $K^\pm \pi^\mp$ mass range from 750 to 1600 MeV/ c^2 . The analysis uses pp collision data collected with the LHCb detector at centre-of-mass energies of 7 and 8 TeV, corresponding to an integrated luminosity of 3.0 fb⁻¹. Several quasi-two-body decay modes are considered, corresponding to $K^\pm \pi^\mp$ combinations with spin 0, 1 and 2, which are dominated by the $K_0^*(800)^0$ and $K_0^*(1430)^0$, the $K^*(892)^0$ and the $K_2^*(1430)^0$ resonances, respectively. The longitudinal polarisation fraction for the $B_s^0 \rightarrow K^*(892)^0 \bar{K}^*(892)^0$ decay is measured as $f_L = 0.208 \pm 0.032 \pm 0.046$, where the first uncertainty is statistical and the second is systematic. The first measurement of the mixing-induced *CP*-violating phase, $\phi_s^{d\bar{d}}$, in $b \rightarrow d\bar{d}s$ transitions is performed, yielding a value of $\phi_s^{d\bar{d}} = -0.10 \pm 0.13$ (stat) ± 0.14 (syst) rad.

Published in JHEP 03 (2018) 140

© CERN on behalf of the LHCb collaboration, licence CC-BY-4.0.

[†]Authors are listed at the end of this paper.

Table 1: Quasi-two-body decay channels and corresponding polarisation amplitudes contributing to the $B_s^0 \rightarrow (K^+\pi^-)(K^-\pi^+)$ final state in the $K\pi$ mass window from 750 to 1600 MeV/ c^2 . The different contributions are identified by the spin j_1 (j_2) of the $K^+\pi^-$ ($K^-\pi^+$) pair and the helicity h . In cases where more than one amplitude contributes, the polarisations are defined as being longitudinal, parallel, or perpendicular, which are then denoted by 0, \parallel and \perp respectively, following the definitions given in Ref. [15]. The subscripts 1 and 2 in the parallel and perpendicular helicities of the tensor-tensor component denote different spin states leading to a parallel or a perpendicular configuration, as discussed in Appendix A.

Decay	Mode	j_1	j_2	Allowed values of h	Number of amplitudes
$B_s^0 \rightarrow (K^+\pi^-)_0^*(K^-\pi^+)_0^*$	scalar-scalar	0	0	0	1
$B_s^0 \rightarrow (K^+\pi^-)_0^*\bar{K}^*(892)^0$	scalar-vector	0	1	0	1
$B_s^0 \rightarrow K^*(892)^0(K^-\pi^+)_0^*$	vector-scalar	1	0	0	1
$B_s^0 \rightarrow (K^+\pi^-)_0^*\bar{K}_2^*(1430)^0$	scalar-tensor	0	2	0	1
$B_s^0 \rightarrow K_2^*(1430)^0(K^-\pi^+)_0^*$	tensor-scalar	2	0	0	1
$B_s^0 \rightarrow K^*(892)^0\bar{K}^*(892)^0$	vector-vector	1	1	0, \parallel , \perp	3
$B_s^0 \rightarrow K^*(892)^0\bar{K}_2^*(1430)^0$	vector-tensor	1	2	0, \parallel , \perp	3
$B_s^0 \rightarrow K_2^*(1430)^0\bar{K}^*(892)^0$	tensor-vector	2	1	0, \parallel , \perp	3
$B_s^0 \rightarrow K_2^*(1430)^0\bar{K}_2^*(1430)^0$	tensor-tensor	2	2	0, \parallel_1 , \perp_1 , \parallel_2 , \perp_2	5

is appropriate. Consequently, such a wide window provides a four-fold increase of the signal sample size with respect to the narrow window of 150 MeV/ c^2 around the K^{*0} mass. The analysis uses pp collision data collected by LHCb in 2011 and 2012 at $\sqrt{s} = 7$ and 8 TeV, corresponding to an integrated luminosity of 3.0 fb $^{-1}$. In this study, nine different quasi-two-body decay channels are considered, corresponding to the different possible combinations of $K\pi$ pairs with spin 0, 1 or 2. Additional contributions were studied and found to be negligible in the phase-space region considered in this analysis. The $K\pi$ spectrum is dominated by the $K_0^*(800)^0$, $K_0^*(1430)^0$, $K^*(892)^0$ and $K_2^*(1430)^0$ resonances. Angular momentum conservation in the decay allows for one single amplitude in modes involving at least one scalar $K\pi$ pair, three amplitudes for vector-vector or vector-tensor decays and five amplitudes for a tensor-tensor decay. These possibilities are listed in Table 1. There is a physical difference between decay pairs of the form scalar-vector and vector-scalar. Namely, in the used convention, the spectator quark from the B_s^0 decay (see Fig. 1) always ends up in the second $K\pi$ pair. The CP -averaged fractions of the contributing amplitudes, f_i , as well as their strong-phase differences, δ_i , are determined together with the CP -violating weak phase $\phi_s^{d\bar{d}}$ and a parameter that accounts for the amount of CP violation in decay, $|\lambda|$. This is the first time that the weak phase in $b \rightarrow d\bar{d}s$ transitions has been measured. It is also the first time that the tensor components in the $(K^+\pi^-)(K^-\pi^+)$ system have been studied.

2 Phenomenology

The phenomenon of quark mixing means that a B_s^0 meson can oscillate into its antiparticle equivalent, \bar{B}_s^0 . Consequently, the physical states, $B_{s,H}^0$ (heavy) and $B_{s,L}^0$ (light), which have mass and decay width differences defined by $\Delta m_s = m_{B_{s,H}^0} - m_{B_{s,L}^0}$ and $\Delta \Gamma_s = \Gamma_{B_{s,L}^0} - \Gamma_{B_{s,H}^0}$, respectively, are admixtures of the flavour eigenstates such that

$$B_{s,H}^0 = pB_s^0 + q\bar{B}_s^0 \quad \text{and} \quad B_{s,L}^0 = pB_s^0 - q\bar{B}_s^0, \quad (1)$$

where p and q are complex coefficients that satisfy $|p|^2 + |q|^2 = 1$. The time evolution of the initially pure flavour eigenstates at $t = 0$, $|B_s^0(0)\rangle$ and $|\bar{B}_s^0(0)\rangle$, is described by

$$\begin{aligned} |B_s^0(t)\rangle &= g_+(t)|B_s^0(0)\rangle + \frac{q}{p}g_-(t)|\bar{B}_s^0(0)\rangle, \\ |\bar{B}_s^0(t)\rangle &= \frac{p}{q}g_-(t)|B_s^0(0)\rangle + g_+(t)|\bar{B}_s^0(0)\rangle, \end{aligned} \quad (2)$$

where the decay-time-dependent functions $g_{\pm}(t)$ are given by

$$g_{\pm}(t) = \frac{1}{2}e^{-im_s t}e^{-\frac{\Gamma_s}{2}t} \left(e^{i\frac{\Delta m_s}{2}t}e^{-\frac{\Delta \Gamma_s}{4}t} \pm e^{-i\frac{\Delta m_s}{2}t}e^{\frac{\Delta \Gamma_s}{4}t} \right), \quad (3)$$

with m_s and Γ_s being the average mass and width of the $B_{s,H}^0$ and $B_{s,L}^0$ states. Negligible CP violation in mixing is assumed in this analysis, leading to the parameterisation $q/p = e^{-i\phi_M}$, where ϕ_M is the B_s^0 - \bar{B}_s^0 mixing phase. The total decay amplitude of the flavour eigenstates at $t = 0$ into the final state $f = (K^+\pi^-)(K^-\pi^+)$, denoted by $\langle f|B_s^0(0)\rangle$ and $\langle f|\bar{B}_s^0(0)\rangle$, is a coherent sum of scalar-scalar (SS), scalar-vector (SV), vector-scalar (VS), scalar-tensor (ST), tensor-scalar (TS), vector-vector (VV), vector-tensor (VT), tensor-vector (TV) and tensor-tensor (TT) contributions. The quantum numbers used to label the $(K^+\pi^-)(K^-\pi^+)$ final states are the spin j_1 (j_2) of the $K^+\pi^-$ ($K^-\pi^+$) pair and the helicity h . The vector component is represented in this analysis by the K^{*0} meson, since this resonance is found to be largely dominant in this spin configuration. Potential contributions from the $K_1^*(1410)^0$ and $K_1^*(1680)^0$ resonances are considered as sources of systematic uncertainty. For the tensor case, only the $K_2^*(1430)^0$ resonance contributes in the considered $K\pi$ mass window. The scalar component, denoted in this paper by $(K\pi)_0^*$ requires a more careful treatment. It can have contributions from the $K_0^*(800)^0$ and $K_0^*(1430)^0$ resonances and from a nonresonant $K\pi$ component. The parameterisation of the $K\pi$ invariant mass spectrum for the scalar contribution is explained later in this section. All of the considered decay modes, together with the quantum numbers for the corresponding amplitudes, are shown in Table 1. In order to separate components with different CP eigenvalues, $\eta_h^{j_1 j_2} = \pm 1$, the differential decay rate is expressed as a function of three angles and the two $K\pi$ invariant masses. The angles θ_1 , θ_2 and φ , are written in the helicity basis and defined according to the diagram shown in Fig. 2. The invariant mass of the $K^+\pi^-$ pair is denoted as m_1 , while that of the $K^-\pi^+$ pair as m_2 . The symbol Ω is used to represent all three angles and the two invariant masses, $\Omega = (m_1, m_2, \cos \theta_1, \cos \theta_2, \varphi)$. Summing over the possible states and using the partial wave formalism, the decay amplitudes at $t = 0$ can be written as

$$\begin{aligned} \langle f|B_s^0(0)\rangle(\Omega) &= \sum_{j_1, j_2, h} \mathcal{A}_h^{j_1 j_2} \Theta_h^{j_1 j_2}(\cos \theta_1, \cos \theta_2, \varphi) \mathcal{H}_h^{j_1 j_2}(m_1, m_2), \\ \langle f|\bar{B}_s^0(0)\rangle(\Omega) &= \sum_{j_1, j_2, h} \eta_h^{j_1 j_2} \bar{\mathcal{A}}_h^{j_1 j_2} \Theta_h^{j_1 j_2}(\cos \theta_1, \cos \theta_2, \varphi) \mathcal{H}_h^{j_1 j_2}(m_1, m_2). \end{aligned} \quad (4)$$

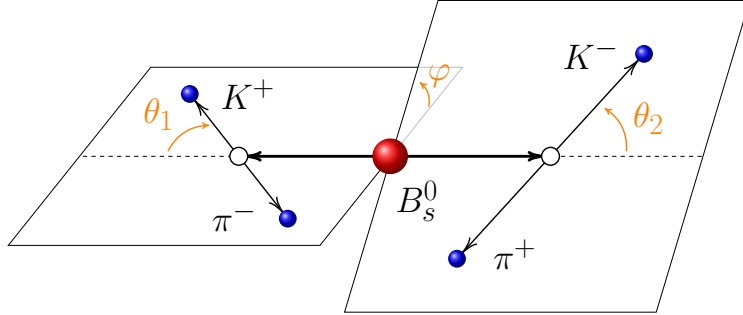


Figure 2: Graphical definition of the angles in the helicity basis. Taking the example of a $B_s^0 \rightarrow Q_1 Q_2$ decay (this analysis uses $B_s^0 \rightarrow SS$, $B_s^0 \rightarrow SV$, $B_s^0 \rightarrow VS$, $B_s^0 \rightarrow VV$, $B_s^0 \rightarrow ST$, $B_s^0 \rightarrow TS$, $B_s^0 \rightarrow VT$, $B_s^0 \rightarrow TV$ and $B_s^0 \rightarrow TT$), with each final-state quasi-two-body meson decaying to pseudoscalars ($Q_1 \rightarrow K^+ \pi^-$ and $Q_2 \rightarrow K^- \pi^+$), θ_1 (θ_2) is defined as the angle between the directions of motion of K^+ (K^-) in the Q_1 (Q_2) rest frame and Q_1 (Q_2) in the B_s^0 rest frame, and φ as the angle between the plane defined by $K^+ \pi^-$ and the plane defined by $K^- \pi^+$ in the B_s^0 rest frame.

The complex parameters $\mathcal{A}_h^{j_1 j_2}$ and $\overline{\mathcal{A}}_h^{j_1 j_2}$ contain the physics of the decays to the final states with j_1 , j_2 and h as defined in Table 1. The angular terms, $\Theta_h^{j_1 j_2}$, are built from combinations of spherical harmonics as shown in Appendix A. The $\eta_h^{j_1 j_2}$ factor is equal to $(-1)^{j_1 + j_2} \eta_h$, where $\eta_h = 1$ for $h \in \{0, \parallel, \parallel_1, \parallel_2\}$ and $\eta_h = -1$ for $h \in \{\perp, \perp_1, \perp_2\}$. The mass-dependent terms are parameterised as

$$\mathcal{H}_h^{j_1 j_2}(m_1, m_2) = \mathcal{F}_h^{j_1 j_2}(m_1, m_2) \mathcal{M}_{j_1}(m_1) \mathcal{M}_{j_2}(m_2), \quad (5)$$

where $\mathcal{F}_h^{j_1 j_2}(m_1, m_2)$ is the Blatt–Weisskopf angular-momentum centrifugal-barrier factor [16] and \mathcal{M}_j describes the shape of the $K\pi$ invariant mass of a $K\pi$ pair with spin j . Relativistic Breit–Wigner functions of spin 1 and 2, parameterising the K^{*0} and the $K_2^*(1430)^0$ resonances, are used for \mathcal{M}_1 and \mathcal{M}_2 , respectively. The parameterisation of \mathcal{M}_0 is based on the phenomenological S -wave scattering amplitude of isospin 1/2 presented in Ref. [17]. Since only the phase evolution of \mathcal{M}_0 is linked to that of the scattering amplitude (by virtue of Watson’s theorem [18]), its modulus is parameterised with a fourth-order polynomial whose coefficients are determined in the final fit to data. Details of this parameterisation can be found in Appendix B. The normalisation condition for the mass-dependent terms is

$$\int dm_1 \int dm_2 |\mathcal{H}_h^{j_1 j_2}(m_1, m_2)|^2 \Phi_4(m_1, m_2) = 1, \quad (6)$$

where Φ_4 is the four-body phase-space factor. The phase of $\mathcal{H}_h^{j_1 j_2}(m_1, m_2)$ is set to 0 at $m_1 = m_2 = M(K^{*0})$, where $M(K^{*0})$ is the mass of the K^{*0} state [15], in order to normalise the relative global phases of the $K\pi$ mass-dependent amplitudes. The CP -violating effects are assumed to be the same for all of the modes under study. Consequently, the value of $\phi_s^{d\bar{d}}$ and $|\lambda|$ determined in this article is effectively an average over the various channels considered in Table 1. Within this approach, the physical amplitudes $\mathcal{A}_h^{j_1 j_2}$ and $\overline{\mathcal{A}}_h^{j_1 j_2}$ in Eq. (4) can be separated into a CP -averaged complex amplitude, $A_h^{j_1 j_2}$, a direct CP asymmetry, $\Delta_{\text{dir}}^{CP} = (|\overline{\mathcal{A}}_h^{j_1 j_2}|^2 - |\mathcal{A}_h^{j_1 j_2}|^2) / (|\overline{\mathcal{A}}_h^{j_1 j_2}|^2 + |\mathcal{A}_h^{j_1 j_2}|^2)$,³ and a CP -violating weak

³The direct CP asymmetry is often notated elsewhere as A_{CP} .

phase in the decay, ϕ_D , as

$$\begin{aligned} \mathcal{A}_h^{j_1 j_2} &= \sqrt{1 - \Delta_{\text{dir}}^{\text{CP}}} e^{-i\phi_D} A_h^{j_1 j_2}, \\ \overline{\mathcal{A}}_h^{j_2 j_1} &= \overline{\mathcal{A}}_h^{j_1 j_2} = \sqrt{1 + \Delta_{\text{dir}}^{\text{CP}}} e^{i\phi_D} A_h^{j_1 j_2}. \end{aligned} \quad (7)$$

In the expressions above the CP transformation also changes $j_1 j_2$ to $j_2 j_1$. The total CP -violating phase associated to the interference between mixing and decay is given by $\phi_s^{d\bar{d}} = \phi_M - 2\phi_D$ and its determination is the main goal of this analysis. In the SM the size of $\phi_s^{d\bar{d}}$ is expected to be small due to an almost exact cancellation in the values of ϕ_M and $2\phi_D$ [5]. The parameter $|\lambda|$ is defined in terms of the direct CP asymmetry by

$$|\lambda| = \frac{\sqrt{1 + \Delta_{\text{dir}}^{\text{CP}}}}{\sqrt{1 - \Delta_{\text{dir}}^{\text{CP}}}}. \quad (8)$$

3 Detector and simulation

The LHCb detector [19, 20] is a single-arm forward spectrometer covering the pseudorapidity range between 2 and 5, designed for the study of particles containing b or c quarks. The detector includes a high-precision tracking system consisting of a silicon-strip vertex detector surrounding the pp interaction region, a large-area silicon-strip detector located upstream of a dipole magnet with a bending power of about 4 Tm, and three stations of silicon-strip detectors and straw drift tubes placed downstream of the magnet. The tracking system provides a measurement of momentum, p , of charged particles with relative uncertainty that varies from 0.5% at low momentum to 1.0% at 200 GeV/ c . The minimum distance of a track to a primary vertex (PV), the impact parameter (IP), is measured with resolution of $(15 + 29/p_T) \mu\text{m}$, where p_T is the component of the momentum transverse to the beam, in GeV/ c . Different types of charged hadrons are distinguished using information from two ring-imaging Cherenkov (RICH) detectors. Photons, electrons and hadrons are identified by a calorimeter system consisting of scintillating-pad and preshower detectors, an electromagnetic calorimeter and a hadronic calorimeter. Muons are identified by a system composed of alternating layers of iron and multiwire proportional chambers. The online event selection is performed by a trigger, which consists of a hardware stage, based on information from the calorimeter and muon systems, followed by a software stage, which applies a full event reconstruction. At the hardware trigger stage, events are required to contain a muon with high p_T or a hadron, photon or electron with high transverse energy in the calorimeters. The software trigger requires a two-, three- or four-track secondary vertex with significant displacement from the primary pp interaction vertices. At least one charged particle must have transverse momentum $p_T > 1.7 \text{ GeV}/c$ and be inconsistent with originating from a PV. A multivariate algorithm [21] is used for the identification of secondary vertices consistent with the decay of a b hadron. Simulated samples of resonant $B_s^0 \rightarrow K^{*0} \bar{K}^{*0}$, $B_s^0 \rightarrow K^{*0} \bar{K}_0^*(1430)^0$ and $B_s^0 \rightarrow K_0^*(1430)^0 \bar{K}_0^*(1430)^0$ decays, as well as phase-space $B_s^0 \rightarrow K^+ \pi^- K^- \pi^+$ decays, are used to study the signal. Simulated samples of $B^0 \rightarrow K^{*0} \bar{K}^{*0}$, $B^0 \rightarrow K^{*0} \rho^0$, $B^0 \rightarrow K^{*0} \phi$ and $\Lambda_b^0 \rightarrow (pK^-)(\pi^+ \pi^-)$ are created to study peaking backgrounds. In the simulation, pp collisions are generated using PYTHIA [22] with a specific LHCb configuration [23]. Decays of particles are described by EVTGEN [24], in which final-state radiation is generated

using PHOTOS [25]. The interaction of the generated particles with the detector, and its response, are implemented using the GEANT4 toolkit [26] as described in Ref. [27].

4 Signal candidate selection

Events passing the trigger are required to satisfy requirements on the fit quality of the B_s^0 decay vertex as well as the p_T and χ_{IP}^2 of each track, where χ_{IP}^2 is defined as the difference between the χ^2 of the secondary vertex reconstructed with and without the track under consideration. The tracks are assigned as kaon or pion candidates using particle identification information from the RICH detectors by requiring that the likelihood for the kaon hypothesis is larger than that for the pion hypothesis and vice versa. In addition, the p_T of each $K\pi$ pair is required to be larger than 500 MeV/c, the reconstructed mass of each $K\pi$ pair is required to be within the range $750 \leq m(K\pi) \leq 1600 \text{ MeV}/c^2$ and the reconstructed mass of the B_s^0 candidate is required to be within the range $5000 \leq m(K^+\pi^-K^-\pi^+) \leq 5800 \text{ MeV}/c^2$. A boosted decision tree (BDT) algorithm [28,29] is trained to reject combinatorial background, where at least one of the final-state tracks originates from a different decay or directly from the PV. The signal is represented in the BDT training with simulated $B_s^0 \rightarrow K^{*0}\bar{K}^{*0}$ candidates, satisfying the same requirements as the data, while selected data candidates in the four-body invariant mass sideband, $5600 \leq m(K^+\pi^-K^-\pi^+) \leq 5800 \text{ MeV}/c^2$, are used to represent the background. The input variables employed in the training are kinematic and geometric quantities associated with the four final-state tracks, the two $K\pi$ candidates and the B_s^0 candidate. The features used to train the BDT response are chosen to minimise any correlation with the B_s^0 and two $K\pi$ pair invariant masses. Separate trainings are performed for the data samples collected in 2011 and 2012, due to the different data-taking conditions. The k -fold cross-validation method [30], with $k = 4$, is used to increase the training statistics while reducing the risk of overtraining. The requirement on the BDT response is optimized by maximising the metric $N_S/\sqrt{N_S + N_B}$, where N_S is the estimated number of signal candidates after selection and N_B is the estimated number of combinatorial background candidates within $\pm 60 \text{ MeV}/c^2$ of the known B_s^0 mass [15]. The BDT requirement is 95% efficient for simulated signal candidates and rejects 70% of the combinatorial background. After applying the BDT requirement, specific background contributions containing two real oppositely charged kaons and two real oppositely charged pions are removed by mass vetoes on the two- and three-body invariant masses. Candidates are removed if they fulfill either $m(K^+K^-\pi^\pm) < 2100 \text{ MeV}/c^2$ or $m(K^+K^-)$ within $30 \text{ MeV}/c^2$ of the known D^0 mass [15]. Sources of peaking background in which one of the final-state tracks is misidentified are suppressed by introducing further particle identification requirements. The particle identification quantities make use of information from the RICH detectors and are calibrated using $D^{*+} \rightarrow D^0\pi^+$ and $\Lambda_b^0 \rightarrow \Lambda_c^+\mu^-\bar{\nu}_\mu$ decays in data. These requirements significantly reduce contributions from $B^0 \rightarrow \rho^0 K^{*0}$, $B^0 \rightarrow \phi K^{*0}$ and $\Lambda_b^0 \rightarrow p\pi^-K^-\pi^+$ in which a pion or proton is misidentified as a kaon, or a kaon is misidentified as a pion. In addition, there are specific extra particle identification requirements for candidates whose reconstructed mass falls within $\pm 30 \text{ MeV}/c^2$ of the known B^0 or Λ_b^0 mass under the relevant mass-hypothesis change ($K \rightarrow p$, $K \rightarrow \pi$ or $\pi \rightarrow K$). These requirements remove 40% of the simulated signal but almost all of the simulated background: 80% of $B^0 \rightarrow \phi K^{*0}$, 96% of $B^0 \rightarrow \rho K^{*0}$ and 88% of

Table 2: Yields of the signal decay and the various background components considered in the four-body invariant mass fit. The uncertainties are statistical only. The signal region is defined as $\pm 60 \text{ MeV}/c^2$ from the known B_s^0 meson mass [15].

Channel	Yield	Yield in Signal Region
$B_s^0 \rightarrow (K^+\pi^-)(K^-\pi^+)$	6080 ± 83	6004
$B^0 \rightarrow (K^+\pi^-)(K^-\pi^+)$	1013 ± 49	103
$B^0 \rightarrow (K^+\pi^-)(K^-K^+)$	281 ± 47	1
$B_s^0 \rightarrow (K^+\pi^-)(K^-K^+)$	8 ± 3	4
$B^0 \rightarrow (K^+\pi^-)(\pi^-\pi^+)$	57 ± 13	33
$\Lambda_b^0 \rightarrow (p\pi^-)(K^-\pi^+)$	44 ± 10	13
Partially reconstructed	2580 ± 151	0
Combinatorial	2810 ± 214	372

$\Lambda_b^0 \rightarrow p\pi^-K^-\pi^+$ events. Subsequently, each of these background components is found to have a small effect on the signal determination. After all of the selection criteria have been imposed, 1.4% of selected events contain multiple candidates, from which one is randomly selected. A fit to the four-body invariant mass distribution is performed in order to determine a set of signal weights, obtained using the *sPlot* procedure [31], which allows the decay-time-dependent *CP* fit to be performed on a sample that represents only the signal. For the invariant mass fit the $B_s^0 \rightarrow (K^+\pi^-)(K^-\pi^+)$ signal and the peaking background components $B^0 \rightarrow (K^+\pi^-)(K^-\pi^+)$, $B_{(s)}^0 \rightarrow (K^+K^-)(K^-\pi^+)$, $B^0 \rightarrow (\pi^+\pi^-)(K^-\pi^+)$ and $\Lambda_b^0 \rightarrow (p\pi^-)(K^-\pi^+)$ are modelled as *Ipatia* functions [32] in which the tail parameters are fixed to values obtained from fits to the simulated samples. The mass difference between the B_s^0 and B^0 mesons is fixed to its known value whilst the mean of the B_s^0 component, as well as the width of both the B^0 and B_s^0 components, are allowed to vary freely. The yields of the $B_s^0 \rightarrow (K^+\pi^-)(K^-\pi^+)$, $B^0 \rightarrow (K^+\pi^-)(K^-\pi^+)$ and $B^0 \rightarrow (K^+K^-)(K^-\pi^+)$ components are allowed to freely vary, whilst the yields of the other components are Gaussian constrained to values relative to the known $B^0 \rightarrow (K^+K^-)(K^-\pi^+)$ branching fraction taking into account the relevant production fractions [33] and reconstruction efficiencies. There is an additional background contribution in the low-mass region from partially reconstructed *b*-hadron decays in which a pion is missed in the final state. This component is modelled as an *ARGUS* function [34] convolved with a Gaussian mass resolution function. The *ARGUS* cutoff parameter is fixed to the fitted B_s^0 mass minus the neutral pion mass, with the other parameters and yield allowed to vary. The combinatorial background is modelled as an exponential function whose shape parameter and yield are allowed to vary. The result of the four-body invariant mass fit, which is used to obtain the *sPlot* signal weights, is shown in Fig. 3. The two $K\pi$ pair invariant masses, with the signal weights applied, are shown in Fig. 4. The resulting yields of the various fit components are shown in Table 2.

5 Flavour tagging

At the LHC, *b* quarks are predominantly produced in $b\bar{b}$ pairs. This analysis focuses on events where one of the quarks hadronises to produce the B_s^0 meson while the other

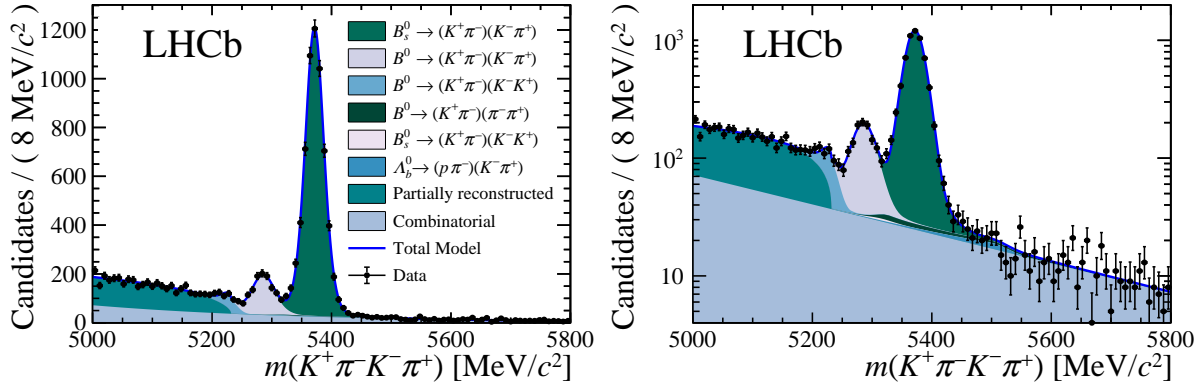


Figure 3: Four-body invariant mass distribution on a (left) linear and (right) logarithmic scale superimposed with the mass fit model.

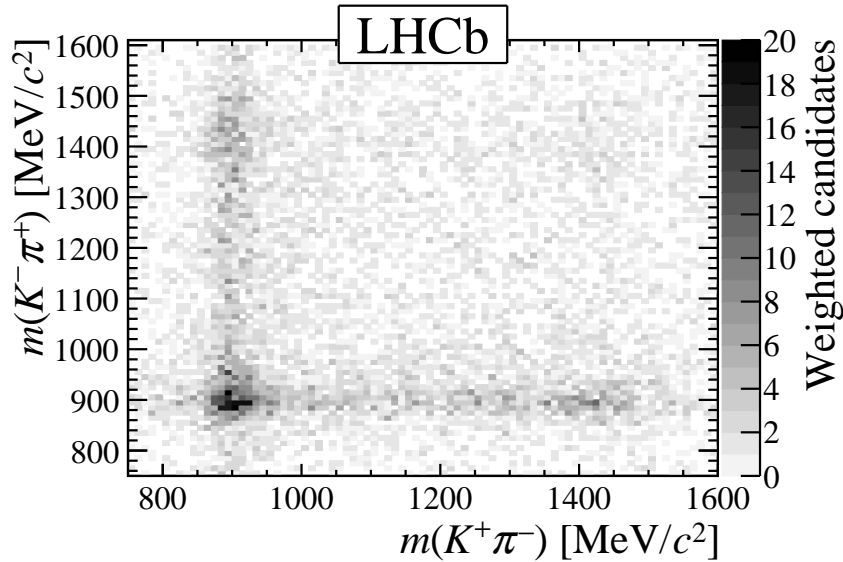


Figure 4: Distribution of the two $(K\pi)$ pair invariant masses, with the signal weights applied, after all of the selection requirements.

quark hadronises and decays independently. Taking advantage of this effect, two types of tagging algorithms aimed at identifying the b -quark flavour at production time are used in this analysis: same-side (SS) taggers, based on information from accompanying particles associated with the signal B_s^0 hadronisation process; and opposite-side (OS) taggers, based on particles produced in the decay of the other b quark. This analysis uses the neural-network-based SS-kaon tagging algorithm presented in Ref. [35]; and the combination of OS tagging algorithms explained in Ref. [36], based on information from b -hadron decays to electrons, muons or kaons and the total charge of tracks that form a vertex. Both the SS and OS tagging algorithms provide for each event a tagging decision, \mathbf{q} , and an estimated mistag probability, η_{tag} . The tagging decision takes the value 1 for B_s^0 , -1 for \bar{B}_s^0 and 0 for untagged. To obtain the calibrated mistag probability for a B_s^0 (\bar{B}_s^0) meson, ω ($\bar{\omega}$), the estimated probability is calibrated on several flavour-specific control

Table 3: The flavour-tagging performance of the SS and OS tagging algorithms, as well as the combination of both, for the signal data sample used in the analysis. The quoted uncertainty includes both statistical and systematic contributions.

Tagging algorithm	ϵ_{tag} [%]	ϵ_{eff} [%]
SS	62.0 ± 0.7	1.63 ± 0.21
OS	37.1 ± 0.7	3.70 ± 0.21
Combination	75.6 ± 0.6	5.15 ± 0.14

channels. The following linear functions are used in the calibration

$$\begin{aligned}\omega^X(\eta_{\text{tag}}^X) &= \left(p_0^X + \frac{\Delta p_0^X}{2}\right) + \left(p_1^X + \frac{\Delta p_1^X}{2}\right) (\eta_{\text{tag}}^X - \langle \eta_{\text{tag}}^X \rangle), \\ \bar{\omega}^X(\eta_{\text{tag}}^X) &= \left(p_0^X - \frac{\Delta p_0^X}{2}\right) + \left(p_1^X - \frac{\Delta p_1^X}{2}\right) (\eta_{\text{tag}}^X - \langle \eta_{\text{tag}}^X \rangle),\end{aligned}\tag{9}$$

where $X \in \{\text{OS}, \text{SS}\}$, $\langle \eta_{\text{tag}}^X \rangle$ is the mean η_{tag}^X of the sample, $p_{0,1}^X$ correspond to calibration parameters averaged over B_s^0 and \bar{B}_s^0 , and $\Delta p_{0,1}^X$ account for B_s^0 and \bar{B}_s^0 asymmetries in the calibration. Among other modes, the portability of the SS tagger calibration was checked on $B_s^0 \rightarrow \phi\phi$ decays [35], which are kinematically similar to the considered signal mode. The tagging efficiency, ϵ_{tag} , denotes the fraction of candidates with a nonzero tagging decision. The tagging power of the sample, $\epsilon_{\text{eff}} = \epsilon_{\text{tag}}(1 - 2\langle\omega\rangle)^2$, characterises the tagging performance. Information from the SS and OS algorithms is combined on a per-event basis (see Eq. (13)) for the decay-time-dependent amplitude fit discussed in Sec. 7. The overall effective tagging power is found to be $(5.15 \pm 0.14)\%$. The flavour-tagging performance is shown in Table 3. When separating the \bar{B}_s^0 and B_s^0 components at $t = 0$, the value of the production asymmetry $A_p = [\sigma(\bar{B}_s^0) - \sigma(B_s^0)]/[\sigma(\bar{B}_s^0) + \sigma(B_s^0)]$, where $\sigma(B_s^0)$ ($\sigma(\bar{B}_s^0)$) is the production cross-section for the B_s^0 (\bar{B}_s^0) meson, also has to be incorporated in the model. This asymmetry was measured by LHCb in pp collisions at $\sqrt{s} = 7$ TeV by means of a decay-time-dependent analysis of $B_s^0 \rightarrow D_s^- \pi^+$ decays [37]. To correct for the different kinematics of $B_s^0 \rightarrow D_s^- \pi^+$ and $B_s^0 \rightarrow (K^+ \pi^-)(K^- \pi^+)$ decays, a weighting in bins of B_s^0 transverse momentum and pseudorapidity is performed, yielding a value of $A_p = -0.005 \pm 0.019$. No detection asymmetry need be considered in this analysis since the final state under consideration is charge symmetric.

6 Acceptance and resolution effects

The LHCb geometrical coverage and selection procedure induce acceptance effects that depend on the three decay angles, the $K\pi$ two-body invariant masses and the decay time. In addition, imperfect reconstruction gives rise to resolution effects. Any deviations caused by imperfect angular and mass resolution are small and are accounted for within the evaluation of systematic uncertainties (see Sec. 8). However, knowledge of the decay-time resolution is of key importance in the determination of $\phi_s^{d\bar{d}}$ and is consequently included in the decay-time-dependent fit. In this analysis, both acceptance and resolution effects are studied using samples of simulated events which have been weighted to match the

data distributions in several important kinematic variables. In the description of the acceptance, the decay-time-dependent part is factorised with respect to the part that depends on the kinematic quantities, since they are found to be only 5% correlated. The acceptance and the decay-time resolutions are determined from simulated events that contain an appropriate combination of the vector-vector $B_s^0 \rightarrow K^{*0} \bar{K}^{*0}$ component with a sample of $B_s^0 \rightarrow K^+ \pi^- K^- \pi^+$ decays generated according to a phase-space distribution. This combination sufficiently populates the phase-space regions to represent the signal decay. To obtain the acceptance function, the simulated events are weighted by the inverse of the probability density function (PDF) used for generation (defined in terms of angles, masses and decay time). The decay-time acceptance is treated analytically and parameterised using cubic spline functions, following the procedure outlined in Ref. [38], with the number of knots chosen to be six. The effect of this choice is addressed as a systematic uncertainty in Sec. 8. The decay-time acceptance is shown in Fig. 5 (bottom right). The five-dimensional kinematic acceptance in angles and masses is included by using normalisation weights in the denominator of the PDF used in the fit to the data, following the procedure described in Ref. [39]. When visualising the fit results (see Fig. 7), the simulated events are weighted using the matrix element of the amplitude fit model. For illustrative purposes, some projections of the kinematic acceptance are shown in Fig. 5. In order to obtain the best possible sensitivity for the measurement of the $\phi_s^{d\bar{d}}$ phase, the time resolution is evaluated event by event, using the estimated decay-time uncertainty, δ_t , obtained in the track reconstruction process. This variable is calibrated using the simulation sample described above to provide the per-event decay-time resolution, σ_t , using a linear relationship

$$\sigma_t(\delta_t) = p_0^{\sigma_t} + p_1^{\sigma_t}(\delta_t - \langle \delta_t \rangle), \quad (10)$$

where $\langle \delta_t \rangle$ is the mean δ_t of the sample and $p_{(0,1)}^{\sigma_t}$ are the calibration parameters. During fitting, σ_t is taken to be the width of a Gaussian resolution function which convolves the decay-time-dependent part of the total amplitude model. Figure 6 shows the relationship between the estimated decay-time uncertainty, δ_t , and the calibrated per-event decay-time resolution, σ_t .

7 Decay-time-dependent amplitude fit

The model used to fit the data is built by taking the squared moduli of the amplitudes $\langle f|B_s^0(t) \rangle$ and $\langle f|\bar{B}_s^0(t) \rangle$ introduced in Sec. 2, multiplying them by the four-body phase-space factor, incorporating the relevant flavour-tagging and production-asymmetry parameters, and including the acceptance and resolution factors obtained in Sec. 6. The observables $\eta_{\text{tag}}^{\text{SS}}$, $\eta_{\text{tag}}^{\text{OS}}$ and δ_t (introduced in Sec. 5 and Sec. 6) are treated as conditional variables. The effective⁴ normalised PDF can be written as

$$\text{PDF}(t, \Omega) = \frac{\sum_{\alpha=1}^{19} \sum_{\beta \leq \alpha} \Re[K_{\alpha\beta}(t) F_{\alpha\beta}(\Omega)]}{\sum_{\alpha'=1}^{19} \sum_{\beta' \leq \alpha'} \Re[(\int dt' K_{\alpha'\beta'}^{\text{untag}}(t') \epsilon_t(t')) \xi_{\alpha'\beta'}]}, \quad (11)$$

⁴In the PDF used for fitting, the marginal PDFs on the conditional variables as well as the acceptance function in the numerator are factored out (see Ref. [39] for details on the acceptance treatment used in this analysis).

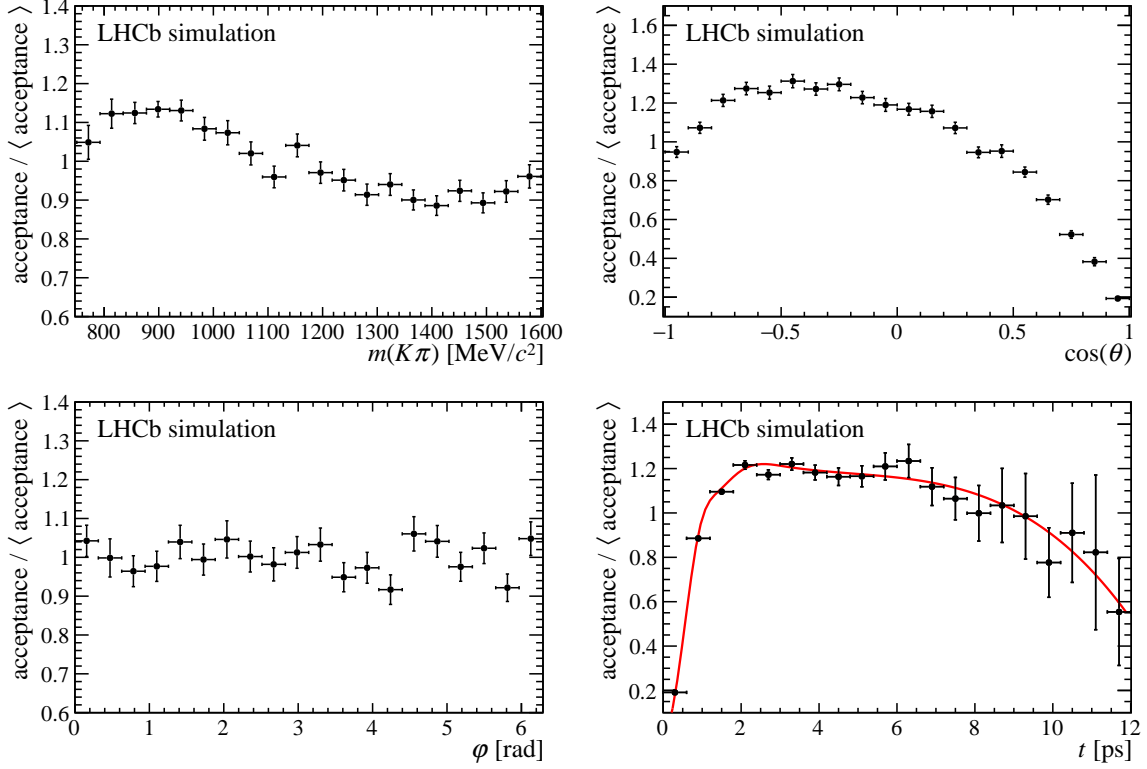


Figure 5: Kinematic acceptance and decay-time distributions evaluated with simulated vector-vector $B_s^0 \rightarrow K^{*0} \bar{K}^{*0}$ and pure phase-space $B_s^0 \rightarrow (K^+ \pi^-)(K^- \pi^+)$ candidates scaled by the mean acceptance. In the bottom right plot the decay-time acceptance obtained from the simulated sample is shown as the black points and the parametric form of the acceptance obtained with cubic splines is shown as the red curve. In the other three plots the black points show the acceptance distribution for the masses and angles. The two $\cos \theta$ variables and the two $m(K\pi)$ masses have been averaged for the purpose of illustration. In the fit, the kinematic acceptance enters via the normalisation weights.

where the subscript α (β) represents the state labels $\{j_1, j_2, h\}$ ($\{j'_1, j'_2, h'\}$), $K_{\alpha\beta}(t)$ parameterises the decay-time dependence and is defined in Eq. (12), and $F_{\alpha\beta}(\Omega)$ are terms that parameterise the angular and mass dependence. Both the numerator and the denominator of Eq. (11) are constructed as a sum over 190 real terms, which arise when squaring the amplitudes decomposed in the combination of the nineteen contributing polarisation states. The decay-time-dependent factors are constructed as

$$K_{\alpha\beta}(t) = R(t, \delta_t) \otimes \left\{ e^{-\Gamma_s t} \left[\zeta_+ \left(a_{\alpha\beta} \cosh \left(\frac{1}{2} \Delta \Gamma_s t \right) + b_{\alpha\beta} \sinh \left(\frac{1}{2} \Delta \Gamma_s t \right) \right) + \zeta_- \left(c_{\alpha\beta} \cos(\Delta m_s t) + d_{\alpha\beta} \sin(\Delta m_s t) \right) \right] \right\}, \quad (12)$$

where $R(t, \delta_t)$ is the decay-time resolution function and the factors ζ_{\pm} contain the flavour-tagging and production-asymmetry information. These factors are

$$\zeta_{\pm} = \frac{(1 + A_p)}{2} P^{\text{OS}}(\mathbf{q}^{\text{OS}}) P^{\text{SS}}(\mathbf{q}^{\text{SS}}) \pm \frac{(1 - A_p)}{2} \bar{P}^{\text{OS}}(\mathbf{q}^{\text{OS}}) \bar{P}^{\text{SS}}(\mathbf{q}^{\text{SS}}), \quad (13)$$

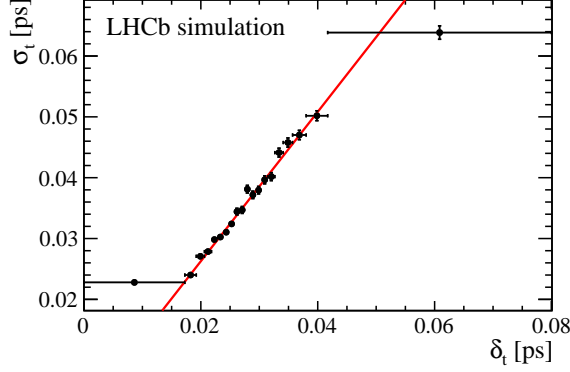


Figure 6: Per-event decay-time resolution, σ_t , versus the estimated per-event decay-time uncertainty, δ_t , obtained from simulated samples containing both vector-vector resonant $B_s^0 \rightarrow K^{*0} \bar{K}^{*0}$ and phase-space $B_s^0 \rightarrow K^+ \pi^- K^- \pi^+$ events.

where

$$\begin{aligned}
 P^X(\mathbf{q}^X) &= \begin{cases} 1 - \omega^X(\eta^X) & \text{for } \mathbf{q}^X = 1, \\ 1 & \text{for } \mathbf{q}^X = 0, \\ \omega^X(\eta^X) & \text{for } \mathbf{q}^X = -1, \end{cases} \\
 \bar{P}^X(\mathbf{q}^X) &= \begin{cases} \bar{\omega}^X(\eta^X) & \text{for } \mathbf{q}^X = 1, \\ 1 & \text{for } \mathbf{q}^X = 0, \\ 1 - \bar{\omega}^X(\eta^X) & \text{for } \mathbf{q}^X = -1, \end{cases}
 \end{aligned} \tag{14}$$

with $X \in \{\text{OS}, \text{SS}\}$. The complex quantities $a_{\alpha\beta}$, $b_{\alpha\beta}$, $c_{\alpha\beta}$ and $d_{\alpha\beta}$ are defined in terms of the CP -averaged amplitudes, the CP -violating parameters and the $\eta_h^{j_1 j_2}$ factors, as

$$\begin{aligned}
 a_{\alpha\beta} &= \frac{2}{1 + |\lambda|^2} \left(A_\alpha A_\beta^* + \eta_\alpha \eta_\beta |\lambda|^2 A_{\bar{\alpha}} A_{\bar{\beta}}^* \right), \\
 b_{\alpha\beta} &= \frac{-2|\lambda|}{1 + |\lambda|^2} \left(\eta_\beta e^{i\phi_s^{d\bar{d}}} A_\alpha A_\beta^* + \eta_\alpha e^{-i\phi_s^{d\bar{d}}} A_{\bar{\alpha}} A_{\bar{\beta}}^* \right), \\
 c_{\alpha\beta} &= \frac{2}{1 + |\lambda|^2} \left(A_\alpha A_\beta^* - \eta_\alpha \eta_\beta |\lambda|^2 A_{\bar{\alpha}} A_{\bar{\beta}}^* \right), \\
 d_{\alpha\beta} &= \frac{-2|\lambda|i}{1 + |\lambda|^2} \left(\eta_\beta e^{i\phi_s^{d\bar{d}}} A_\alpha A_\beta^* - \eta_\alpha e^{-i\phi_s^{d\bar{d}}} A_{\bar{\alpha}} A_{\bar{\beta}}^* \right),
 \end{aligned} \tag{15}$$

where the bars on the amplitude indices α and β denote the CP transformation of the considered final state, *i.e.* the change of quantum numbers $j_1 j_2 \rightarrow j_2 j_1$. The functions $K_{\alpha\beta}^{\text{untag}}$ are obtained by summing $K_{\alpha\beta}$ over the tagging decisions. The angular- and mass-dependent terms are constructed as

$$\begin{aligned}
 F_{\alpha\beta}(\Omega) &= (2 - \delta_{\alpha\beta}) \Theta_h^{j_1 j_2}(\cos \theta_1, \cos \theta_2, \varphi) [\Theta_{h'}^{j_1' j_2'}(\cos \theta_1, \cos \theta_2, \varphi)]^* \\
 &\times \mathcal{M}_{j_1}(m_1) \mathcal{M}_{j_2}(m_2) \mathcal{M}_{j_1'}^*(m_1) \mathcal{M}_{j_2'}^*(m_2) \\
 &\times \mathcal{F}_h^{j_1 j_2}(m_1, m_2) \mathcal{F}_{h'}^{j_1' j_2'}(m_1, m_2) \Phi_4(m_1, m_2),
 \end{aligned} \tag{16}$$

where $\delta_{\alpha\beta}$ is the Kronecker delta and the other terms have been introduced in Sec. 2. The decay-time acceptance function, $\epsilon_t(t)$, and the normalisation weights, $\xi_{\alpha\beta}$, are included in

the denominator of Eq. (11). The normalisation weights correspond to angular and mass integrals that involve the five-dimensional kinematic acceptance, $\epsilon_\Omega(\Omega)$, and are obtained by summing over the events in the simulated sample

$$\xi_{\alpha\beta} \equiv \int d\Omega F_{\alpha\beta}(\Omega) \epsilon_\Omega(\Omega) \propto \sum_i^{N_{\text{events}}} \frac{F_{\alpha\beta}(\Omega_i)}{G(\Omega_i)}, \quad (17)$$

where $G(\Omega)$ is the model used for generation. The CP -conserving amplitudes, $A_h^{j_1, j_2}$, the direct CP -asymmetry parameter, $|\lambda|$, and the mixing induced CP -violating phase, $\phi_s^{d\bar{d}}$, are allowed to vary during the fit. Gaussian constraints are applied to Δm_s , Γ_s and $\Delta\Gamma_s$ from their known values [8], and to the flavour-tagging and decay-time resolution calibration parameters, introduced in Sec. 5 and Sec. 6. The CP -averaged amplitudes are characterised in the fit by wave fractions, f^w , polarisation fractions, f_h^w , and strong phases, δ_h^w , given by

$$\begin{aligned} f^w &= \frac{\sum_h |A_h^w|^2}{\sum_{w'} \sum_{h'} |A_{h'}^{w'}|^2}, \\ f_h^w &= \frac{|A_h^w|^2}{\sum_{h'} |A_{h'}^w|^2}, \\ \delta_h^w &= \arg(A_h^w), \end{aligned} \quad (18)$$

with w running over the nine decays under study and h running over the available helicities for each channel. With these definitions it follows that

$$\sum_w f^w = 1, \quad \sum_h f_h^w = 1, \quad \forall w, \quad (19)$$

so not all the fractions are independent of each other, for example $f_\perp^{VV} = 1 - f_L^{VV} - f_\parallel^{VV}$. The phase of the longitudinal polarisation amplitude of the vector-vector component is set to zero to serve as a reference.

8 Systematic uncertainties

The decay-time-dependent amplitude model and the fit procedure are cross-checked in several independent ways: using purely simulated decays, fitting in a narrow window around the dominant K^{*0} resonance, fitting only in the high-mass region above the K^{*0} resonance, considering higher-spin contributions (whose effect is found to be negligible), ensuring that there is no bias when repeating the fit procedure on ensembles of pseudo-experiments and by repeating the fit on subsamples of the data set split by the year of data taking, the magnet polarity and using a different mass range. These checks give compatible results. Several sources of systematic uncertainty are considered for each of the physical observables extracted in the decay-time-dependent fit. These are described in this section. A summary of the systematic uncertainties is given in Table 4.

8.1 Fit to the four-body invariant mass distribution

The uncertainty on the yield of each of the partially reconstructed components used in the four-body invariant mass fit is propagated to the decay-time-dependent amplitude fit

by recalculating the *sPlot* signal weights after varying each of the yields by one standard deviation. Sources of systematic uncertainty which arise from mismodelling the shapes of both the background and signal components are calculated by performing the full fit procedure using alternative parameterisations. The signal is replaced with a double-sided Crystal Ball function [40] instead of the nominal Ipatia shape described in Sec. 4 and the combinatorial-background shape is replaced with a first-order polynomial instead of the nominal exponential function.

8.2 Weights derived from the *sPlot* procedure

The *sPlot* procedure assumes that there is no correlation between the fit variable used to determine the weights, in this case the four-body invariant mass, $m(K^+\pi^-K^-\pi^+)$, and the projected variables in which the signal distribution is unfolded, in this case the three angles and two masses, Ω . This is checked to be valid to a close approximation for signal decays. In order to assess the impact of any residual correlations in the signal weights, the four-body mass fit is performed by splitting the data into different bins of $\cos\theta$ for each $(K\pi)$ pair. For each subcategory the four-body fit is repeated and the resulting model is used to compute a new set of signal weights for the full sample. The largest difference between each subcategory value and the nominal fit value is taken as the systematic uncertainty.

8.3 Decay-time-dependent fit procedure

An ensemble of pseudoexperiments is generated to estimate the bias on the parameters of the decay-time-dependent fit. For each experiment, a sample with a similar size to the selected signal is generated using the matrix element of the nominal model (employing the measured amplitudes) and then refitted to determine the deviation induced in the fit parameters. The systematic uncertainty is calculated as the mean of the deviation over the ensemble.

8.4 Decay-time-dependent fit parameterisation

Several sources of systematic uncertainty originating from the decay-time-dependent fit model have been studied. These include the parameterisations of the angular momentum centrifugal-barrier factors, the mean and width of the Breit–Wigner functions and the model for the S-wave propagator. An alternative model-independent approach is used, as described in Appendix B. The systematic uncertainties are obtained for each of these cases by comparing the fitted parameter values of the alternative model with the fitted values from the nominal model. Additional contributions from higher mass $(K\pi)$ vector resonances, namely the $K_1^*(1410)^0$ and the $K_1^*(1680)^0$ states, are also considered. In this case, the size of these components is first estimated on data through a simplified fit. Afterwards, an ensemble of pseudoexperiments is generated including these resonances in the model and then refitting with the nominal PDF. The total systematic uncertainty for the decay-time-dependent fit model is taken as the sum in quadrature of these alternatives.

8.5 Acceptance normalisation weights

The kinematic acceptance weights, explained in Sec. 7, are computed from simulated samples of limited size, which induces an uncertainty. This systematic uncertainty is calculated using an ensemble of pseudoexperiments in which the acceptance weights are randomly varied according to their covariance matrix (evaluated on the simulated sample). The root-mean-square of the distribution of the differences between the nominal fitted value and the value obtained in each pseudoexperiment is taken as the size of the systematic uncertainty. This effect is found to be the largest systematic uncertainty impacting the measurement of the $\phi_s^{d\bar{d}}$ phase.

8.6 Other acceptance and resolution effects

Various other acceptance and resolution effects for the decay angles, the two $K\pi$ pair masses and the decay-time are accounted for. Most of these quantities are nominally computed in the decay-time-dependent fit using simulation samples. Any differences between data and simulation are accounted for by the systematic uncertainties described in this section. Furthermore, various other effects originating from mismodelling of the decay-time acceptance and decay-time resolution functions are considered. Each of these effects are summed in quadrature to provide the value listed in Table 4. The kinematic and decay-time acceptances, shown in Fig. 5, are computed from samples of simulated signal events. Small systematic effects can arise due to differences between the data and the simulated samples. In particular, mismodelling of the B_s^0 and the four-track momentum distributions can impact the acceptance in $\cos\theta$. This effect is checked by producing a data-driven correction for the simulation in several relevant physical quantities.⁵ This correction is produced using an iterative procedure that removes any effects arising from differences between the model used in the event generation and the actual decay kinematics of $B_s^0 \rightarrow (K^+\pi^-)(K^-\pi^+)$ decays. The systematic uncertainty is computed as the difference in the fit parameters before and after the iterative correction has been applied. Systematic effects due to the possible mismodelling of the decay-time-dependent acceptance are studied by generating ensembles of pseudoexperiments in two different configurations: one in which the decay-time acceptance spline coefficients are randomised and one in which the configuration of the decay-time acceptance knots is varied. The nominal decay-time-dependent fit procedure is repeated for each pseudoexperiment and the systematic uncertainty for each of these two effects is computed as the average deviation of the fit parameters from their generated values over each ensemble. Sources of systematic uncertainty which affect the decay-time resolution are studied by modifying the calibration function in Eq. (10) that is used to obtain the per-event decay-time resolution. First, the nominal function is substituted by an alternative quadratic form, to assess the effect of nonlinearity in the calibration. Second, the nominal function is multiplied by a scale factor that accounts for possible remaining differences between data and simulation. This scale factor is taken from the analysis of $B_s^0 \rightarrow J/\psi\phi$ decays performed by LHCb in Ref. [41]. In the both cases, the systematic uncertainties are obtained by comparing the values resulting from the alternative configurations with the nominal values. The effect of the resolution on the masses and angles is studied by generating ensembles of

⁵The variables used to correct the distributions of the simulation are the momentum and pseudorapidity of the kaons and pions, the transverse momentum of the B_s^0 and the number of tracks in the event.

pseudoexperiments for which the masses and angles are smeared using a multi-dimensional Gaussian resolution function, obtained from simulation. The systematic uncertainty is computed as the mean deviation between the fitted and generated values.

8.7 Production asymmetry

The uncertainty of the production asymmetry for the B_s^0 meson is studied by computing the maximum difference between the nominal conditions and when the production asymmetry is shifted to $\pm 1\sigma$ of its nominal value.

9 Fit results

An unbinned maximum likelihood fit is applied to the background-subtracted data using the PDF defined in Eq. (11). The large computational load due to the complexity of the fit motivates the parallelisation of the process on a Graphics Processing Unit (GPU), for which the IPANEMA software package [42, 43] is used. The one-dimensional projections of the results in the six analysis variables are shown in Fig. 7 along with the separate components from the contributing decay modes listed in Table 1. The resulting fit values for the common CP observables, $\phi_s^{d\bar{d}}$ and $|\lambda|$, as well as the CP -averaged fractions, f_i , and polarisation strong-phase differences, δ_i , for each component are given in Table 5. The central values are given along with the statistical uncertainties obtained from the fit and the systematic uncertainties, which are discussed in Sec. 8. These are the first measurements in a $b \rightarrow d\bar{d}s$ transition of the CP -violation parameter $|\lambda| = 1.035 \pm 0.034 \pm 0.089$ and the CP -violating weak phase $\phi_s^{d\bar{d}} = -0.10 \pm 0.13 \pm 0.14$ rad. Both are consistent with no CP violation and with the SM predictions. In the region of phase space considered, the $B_s^0 \rightarrow K^{*0}\bar{K}^{*0}$ vector-vector component has a relatively small fraction, of $f^{VV} = 0.067 \pm 0.004 \pm 0.024$, mainly due to the large scalar $K\pi$ contributions. Indeed, a relatively large contribution from the scalar-scalar double S -wave fraction is determined to be $f^{SS} = 0.225 \pm 0.010 \pm 0.069$. The tensor-tensor double D -wave fraction is measured to be $f^{TT} = 0.011 \pm 0.003 \pm 0.007$. The cross-term contributions from the scalar with the vector combination (single S -wave) and the vector with the tensor combination (single D -wave) are also found to be large, $f^{SV} = 0.329 \pm 0.015 \pm 0.071$, $f^{VS} = 0.133 \pm 0.013 \pm 0.065$, $f^{VT} = 0.160 \pm 0.016 \pm 0.049$ and $f^{TV} = 0.036 \pm 0.014 \pm 0.048$, while a small contribution from the scalar with the tensor combination is found, $f^{TS} = 0.025 \pm 0.007 \pm 0.033$ and $f^{ST} = 0.014 \pm 0.006 \pm 0.031$. The values of the longitudinal polarisation fractions of the vector-vector and tensor-tensor components are found to be small, $f_L^{TT} = 0.25 \pm 0.14 \pm 0.18$ and $f_L^{VV} = 0.208 \pm 0.032 \pm 0.046$, while the longitudinal polarisation fractions of the vector with the tensor components are measured to be large, $f_L^{VT} = 0.911 \pm 0.020 \pm 0.165$ and $f_L^{TV} = 0.62 \pm 0.16 \pm 0.25$.

10 Summary

A flavour-tagged decay-time-dependent amplitude analysis of the $B_s^0 \rightarrow (K^+\pi^-)(K^-\pi^+)$ decay, for $(K^\pm\pi^\mp)$ invariant masses in the range from 750 to 1600 MeV/ c^2 , is performed on a data set corresponding to an integrated luminosity of 3.0 fb $^{-1}$ obtained by the LHCb experiment with pp collisions at $\sqrt{s} = 7$ TeV and $\sqrt{s} = 8$ TeV. Several quasi-two-body decay components are considered, corresponding to $(K^\pm\pi^\mp)$ combinations with spins of 0,

Table 4: Summary of the systematic uncertainties on the two CP parameters, the CP -averaged fractions and the strong phase differences (in radians) for each of the components listed in Table 1.

Parameter	ϕ_s^{dd} [rad]	$ \lambda $	f^{VV}	f_L^{VV}	f_{\parallel}^{VV}	δ_{\parallel}^{VV}	δ_{\perp}^{VV}	f^{SV}	f^{VS}	δ^{SV}	δ^{VS}	f^{SS}	δ^{SS}	
Yield and shape of mass model	0.012	0.001	0.001	0.004	0.004	0.011	0.020	0.002	0.003	0.023	0.023	0.004	0.012	
Signal weights of mass model	0.012	0.007	0.002	0.006	0.005	0.024	0.112	0.004	0.005	0.049	0.022	0.005	0.047	
Decay-time-dependent fit procedure	0.006	0.002	0.001	0.006	0.002	0.007	0.017	0.003	0.002	0.007	0.027	0.001	0.009	
Decay-time-dependent fit parameterisation	0.049	0.013	0.021	0.025	0.026	0.187	0.202	0.042	0.029	0.159	0.234	0.064	0.227	
Acceptance weights (simulated sample size)	0.106	0.078	0.004	0.031	0.029	0.236	0.564	0.037	0.039	0.250	0.290	0.015	0.256	
Other acceptance and resolution effects	0.063	0.008	0.005	0.018	0.005	0.136	0.149	0.006	0.004	0.167	0.124	0.017	0.194	
Production asymmetry	0.002	0.002	0.000	0.000	0.000	0.001	0.017	0.002	0.002	0.002	0.008	0.000	0.002	
Total	0.141	0.089	0.024	0.046	0.042	0.333	0.641	0.071	0.065	0.346	0.405	0.069	0.399	
Parameter	f^{ST}	f_L^{ST}	δ^{ST}	f_L^{VT}	f_{\parallel}^{VT}	f_{\perp}^{VT}	f^{TV}	f_L^{TV}	f_{\parallel}^{TV}	f_{\perp}^{TV}	δ_0^{VT}	δ_{\perp}^{VT}	δ_0^{TV}	δ_{\perp}^{TV}
Yield and shape of mass model	0.002	0.004	0.111	0.023	0.001	0.003	0.001	0.001	0.043	0.025	0.023	0.055	0.110	0.053
Signal weights of mass model	0.004	0.006	0.151	0.105	0.002	0.003	0.001	0.001	0.043	0.029	0.025	0.131	0.126	0.080
Decay-time-dependent fit procedure	0.001	0.002	0.248	0.017	0.002	0.004	0.002	0.002	0.008	0.005	0.012	0.069	0.025	0.062
Decay-time-dependent fit parameterisation	0.006	0.017	0.736	0.247	0.011	0.053	0.019	0.008	0.080	0.048	0.286	0.308	0.260	0.228
Acceptance weights (simulated sample size)	0.014	0.015	1.463	0.719	0.026	0.145	0.054	0.027	0.199	0.102	1.117	1.080	0.888	0.712
Other acceptance and resolution effects	0.002	0.003	0.184	0.226	0.015	0.024	0.004	0.005	0.045	0.017	0.163	0.168	0.191	0.229
Production asymmetry	0.001	0.001	0.037	0.026	0.001	0.003	0.001	0.002	0.012	0.006	0.015	0.030	0.018	0.003
Total	0.031	0.033	1.688	0.817	0.049	0.165	0.063	0.048	0.252	0.143	1.171	1.159	0.970	0.802
Parameter	f^{TT}	f_L^{TT}	f_{\parallel}^{TT}	f_{\perp}^{TT}	f_{\parallel}^{TT}	δ_0^{TT}	δ_{\parallel}^{TT}	δ_{\perp}^{TT}	$\delta_{\perp_1}^{TT}$	$\delta_{\perp_2}^{TT}$	$\delta_{\perp_1}^{TV}$	$\delta_{\perp_2}^{TV}$		
Yield and shape of mass model	0.000	0.045	0.019	0.037	0.002	0.038	0.027	0.009	0.079	0.114				
Signal weights of mass model	0.000	0.066	0.025	0.024	0.002	0.147	0.046	0.112	0.123	0.215				
Decay-time-dependent fit procedure	0.001	0.022	0.022	0.014	0.004	0.127	0.036	0.068	0.058	0.040				
Decay-time-dependent fit parameterisation	0.005	0.051	0.071	0.113	0.038	1.213	0.199	0.685	0.820	0.476				
Acceptance weights (simulated sample size)	0.003	0.135	0.110	0.127	0.077	1.328	0.454	1.348	1.443	1.161				
Other acceptance and resolution effects	0.002	0.031	0.028	0.056	0.024	0.226	0.275	0.156	0.343	0.301				
Production asymmetry	0.000	0.002	0.001	0.008	0.003	0.005	0.002	0.062	0.015	0.043				
Total	0.007	0.176	0.142	0.205	0.107	1.825	0.573	1.546	1.706	1.330				

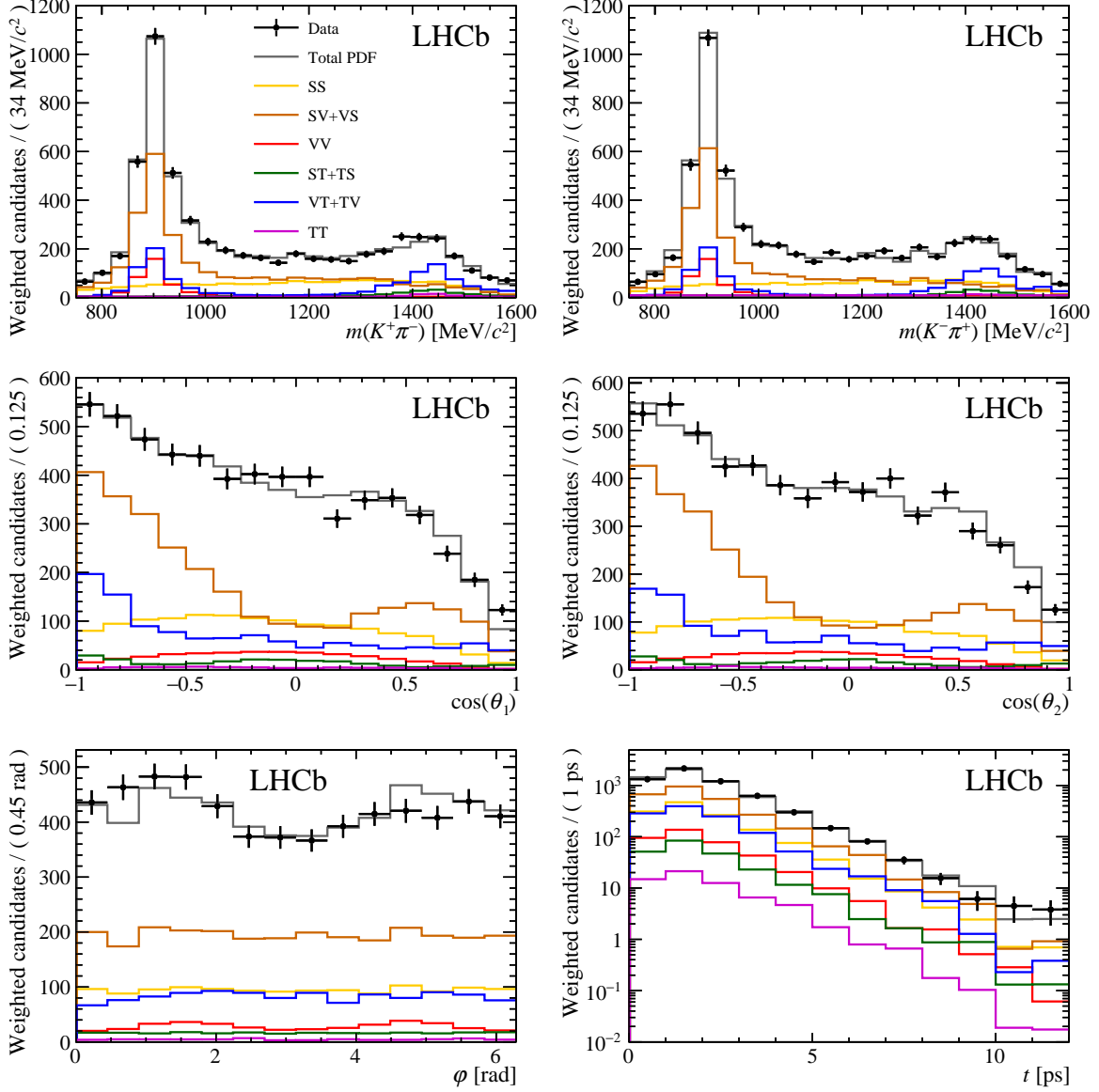


Figure 7: One-dimensional projections of the decay-time-dependent, flavour-tagged fit to (black points) the $sPlot$ weighted data for (top row) the two $(K\pi)$ invariant masses, (middle row) the two $(K\pi)$ decay plane angles, (bottom left) the angle between the two (K, π) decay planes and (bottom right) the decay-time. The solid gray line represents the total fit model along with the CP -averaged components for each contributing decay.

1 and 2. The longitudinal polarisation fraction for the $B_s^0 \rightarrow K^{*0} \bar{K}^{*0}$ vector-vector decay is determined to be $f_L^{VV} = 0.208 \pm 0.032 \pm 0.046$, where the first uncertainty is statistical and the second one systematic. This confirms, with improved precision, the relatively low value reported previously by LHCb [14]. The first determination of the CP asymmetry of the $(K^+\pi^-)(K^-\pi^+)$ final state and the best, sometimes the first, measurements of 19 CP -averaged amplitude parameters corresponding to scalar, vector and tensor final states, are also reported. This analysis determines for the first time the mixing-induced CP -violating phase ϕ_s using a $b \rightarrow \bar{d}\bar{d}s$ transition. The value of this phase is measured to be $\phi_s^{\bar{d}\bar{d}} = -0.10 \pm 0.13 \pm 0.14$ rad, which is consistent with both the SM expectation [7]

Table 5: Results of the decay-time-dependent amplitude fit to data. The first uncertainty is statistical and the second uncertainty is systematic.

Parameter	Value	Parameter	Value
Common parameters		Vector/Tensor (VT and TV)	
$\phi_s^{d\bar{d}}$ [rad]	$-0.10 \pm 0.13 \pm 0.14$	f^{VT}	$0.160 \pm 0.016 \pm 0.049$
$ \lambda $	$1.035 \pm 0.034 \pm 0.089$	f_L^{VT}	$0.911 \pm 0.020 \pm 0.165$
Vector/Vector (VV)		f_{\parallel}^{VT}	$0.012 \pm 0.008 \pm 0.053$
f^{VV}	$0.067 \pm 0.004 \pm 0.024$	f^{TV}	$0.036 \pm 0.014 \pm 0.048$
f_L^{VV}	$0.208 \pm 0.032 \pm 0.046$	f_L^{TV}	$0.62 \pm 0.16 \pm 0.25$
f_{\parallel}^{VV}	$0.297 \pm 0.029 \pm 0.042$	f_{\parallel}^{TV}	$0.24 \pm 0.10 \pm 0.14$
δ_{\parallel}^{VV} [rad]	$2.40 \pm 0.11 \pm 0.33$	δ_0^{VT} [rad]	$-2.06 \pm 0.19 \pm 1.17$
δ_{\perp}^{VV} [rad]	$2.62 \pm 0.26 \pm 0.64$	δ_{\parallel}^{VT} [rad]	$-1.8 \pm 0.4 \pm 1.0$
Scalar/Vector (SV and VS)		δ_{\perp}^{VT} [rad]	$-3.2 \pm 0.3 \pm 1.2$
f^{SV}	$0.329 \pm 0.015 \pm 0.071$	δ_0^{TV} [rad]	$1.91 \pm 0.30 \pm 0.80$
f^{VS}	$0.133 \pm 0.013 \pm 0.065$	δ_{\parallel}^{TV} [rad]	$1.09 \pm 0.19 \pm 0.55$
δ^{SV} [rad]	$-1.31 \pm 0.10 \pm 0.35$	δ_{\perp}^{TV} [rad]	$0.2 \pm 0.4 \pm 1.1$
δ^{VS} [rad]	$1.86 \pm 0.11 \pm 0.41$	Tensor/Tensor (TT)	
Scalar/Scalar (SS)		f^{TT}	$0.011 \pm 0.003 \pm 0.007$
f^{SS}	$0.225 \pm 0.010 \pm 0.069$	f_L^{TT}	$0.25 \pm 0.14 \pm 0.18$
δ^{SS} [rad]	$1.07 \pm 0.10 \pm 0.40$	$f_{\parallel 1}^{TT}$	$0.17 \pm 0.11 \pm 0.14$
Scalar/Tensor (ST and TS)		$f_{\perp 1}^{TT}$	$0.30 \pm 0.18 \pm 0.21$
f^{ST}	$0.014 \pm 0.006 \pm 0.031$	$f_{\parallel 2}^{TT}$	$0.015 \pm 0.033 \pm 0.107$
f^{TS}	$0.025 \pm 0.007 \pm 0.033$	δ_0^{TT} [rad]	$1.3 \pm 0.5 \pm 1.8$
δ^{ST} [rad]	$-2.3 \pm 0.4 \pm 1.7$	$\delta_{\parallel 1}^{TT}$ [rad]	$3.00 \pm 0.29 \pm 0.57$
δ^{TS} [rad]	$-0.10 \pm 0.26 \pm 0.82$	$\delta_{\perp 1}^{TT}$ [rad]	$2.6 \pm 0.4 \pm 1.5$
		$\delta_{\parallel 2}^{TT}$ [rad]	$2.3 \pm 0.8 \pm 1.7$
		$\delta_{\perp 2}^{TT}$ [rad]	$0.7 \pm 0.6 \pm 1.3$

and the corresponding LHCb result of $\phi_s^{s\bar{s}} = -0.17 \pm 0.15 \pm 0.03$ rad measured using $B_s^0 \rightarrow \phi\phi$ decays [12]. The statistical uncertainty of the two measurements is at a similar level although the systematic uncertainty of this measurement is larger, which is mainly due to the treatment of the multi-dimensional acceptance. It is expected that this can be reduced by increasing the size of the simulation sample used to determine the acceptance effects. Most other sources of systematic uncertainty are expected to scale with larger data samples.

Acknowledgements

We express our gratitude to our colleagues in the CERN accelerator departments for the excellent performance of the LHC. We thank the technical and administrative staff at the LHCb institutes. We acknowledge support from CERN and from the national agencies: CAPES, CNPq, FAPERJ and FINEP (Brazil); MOST and NSFC (China); CNRS/IN2P3 (France); BMBF, DFG and MPG (Germany); INFN (Italy); NWO (The Netherlands); MNiSW and NCN (Poland); MEN/IFA (Romania); MinES and FASO (Russia); MinECo (Spain); SNSF and SER (Switzerland); NASU (Ukraine); STFC (United Kingdom); NSF (USA). We acknowledge the computing resources that are provided by CERN, IN2P3 (France), KIT and DESY (Germany), INFN (Italy), SURF (The Netherlands), PIC (Spain), GridPP (United Kingdom), RRCKI and Yandex LLC (Russia), CSCS (Switzerland), IFIN-HH (Romania), CBPF (Brazil), PL-GRID (Poland) and OSC (USA). We are indebted to the communities behind the multiple open-source software packages on which we depend. Individual groups or members have received support from AvH Foundation (Germany), EPLANET, Marie Skłodowska-Curie Actions and ERC (European Union), ANR, Labex P2IO and OCEVU, and Région Auvergne-Rhône-Alpes (France), RFBR, RSF and Yandex LLC (Russia), GVA, XuntaGal and GENCAT (Spain), Herchel Smith Fund, the Royal Society, the English-Speaking Union and the Leverhulme Trust (United Kingdom).

Appendices

A Angular distributions

The angular dependence of the decay amplitudes introduced in Eq. (4) is shown in Table 6.

Table 6: Functions containing the angular dependence of the amplitudes, as introduced in Eq. (4). For a discussion on some of the angular terms see Ref. [7].

j_1	j_2	h	$Y_{\ell_1}^{m_1}(\theta_1, -\varphi)Y_{\ell_2}^{m_2}(\pi - \theta_2, 0)$	$\Theta_h^{j_1 j_2}(\cos \theta_1, \cos \theta_2, \varphi)$
0	0	0	$\sqrt{\pi}Y_0^0Y_0^0$	$\frac{1}{2\sqrt{2\pi}}$
0	1	0	$\sqrt{\pi}Y_0^0Y_1^0$	$-\frac{\sqrt{3}}{2\sqrt{2\pi}}\cos\theta_2$
1	0	0	$\sqrt{\pi}Y_1^0Y_0^0$	$\frac{\sqrt{3}}{2\sqrt{2\pi}}\cos\theta_1$
0	2	0	$\sqrt{\pi}Y_0^0Y_2^0$	$\frac{\sqrt{5}}{4\sqrt{2\pi}}(3\cos^2\theta_2 - 1)$
2	0	0	$\sqrt{\pi}Y_2^0Y_0^0$	$\frac{\sqrt{5}}{4\sqrt{2\pi}}(3\cos^2\theta_1 - 1)$
1	1	0	$\sqrt{\pi}Y_1^0Y_1^0$	$-\frac{3}{2\sqrt{2\pi}}\cos\theta_1\cos\theta_2$
1	1	\parallel	$\frac{\sqrt{\pi}}{\sqrt{2}}(Y_1^{-1}Y_1^{+1} + Y_1^{+1}Y_1^{-1})$	$-\frac{3}{4\sqrt{\pi}}\sin\theta_1\sin\theta_2\cos\varphi$
1	1	\perp	$\frac{\sqrt{\pi}}{\sqrt{2}}(Y_1^{-1}Y_1^{+1} - Y_1^{+1}Y_1^{-1})$	$-i\frac{3}{4\sqrt{\pi}}\sin\theta_1\sin\theta_2\sin\varphi$
1	2	0	$\sqrt{\pi}Y_1^0Y_2^0$	$\frac{\sqrt{15}}{4\sqrt{2\pi}}\cos\theta_1(3\cos^2\theta_2 - 1)$
1	2	\parallel	$\frac{\sqrt{\pi}}{\sqrt{2}}(Y_1^{-1}Y_2^{+1} + Y_1^{+1}Y_2^{-1})$	$\frac{3\sqrt{5}}{4\sqrt{\pi}}\sin\theta_1\sin\theta_2\cos\theta_2\cos\varphi$
1	2	\perp	$\frac{\sqrt{\pi}}{\sqrt{2}}(Y_1^{-1}Y_2^{+1} - Y_1^{+1}Y_2^{-1})$	$i\frac{3\sqrt{5}}{4\sqrt{\pi}}\sin\theta_1\sin\theta_2\cos\theta_2\sin\varphi$
2	1	0	$\sqrt{\pi}Y_2^0Y_1^0$	$-\frac{\sqrt{15}}{4\sqrt{2\pi}}(3\cos^2\theta_1 - 1)\cos\theta_2$
2	1	\parallel	$\frac{\sqrt{\pi}}{\sqrt{2}}(Y_2^{-1}Y_1^{+1} + Y_2^{+1}Y_1^{-1})$	$-\frac{3\sqrt{5}}{4\sqrt{\pi}}\sin\theta_1\cos\theta_1\sin\theta_2\cos\varphi$
2	1	\perp	$\frac{\sqrt{\pi}}{\sqrt{2}}(Y_2^{-1}Y_1^{+1} - Y_2^{+1}Y_1^{-1})$	$-i\frac{3\sqrt{5}}{4\sqrt{\pi}}\sin\theta_1\cos\theta_1\sin\theta_2\sin\varphi$
2	2	0	$\sqrt{\pi}Y_2^0Y_2^0$	$\frac{5}{8\sqrt{2\pi}}(3\cos^2\theta_1 - 1)(3\cos^2\theta_2 - 1)$
2	2	\parallel_1	$\frac{\sqrt{\pi}}{\sqrt{2}}(Y_2^{-1}Y_2^{+1} + Y_2^{+1}Y_2^{-1})$	$\frac{15}{4\sqrt{\pi}}\sin\theta_1\cos\theta_1\sin\theta_2\cos\theta_2\cos\varphi$
2	2	\perp_1	$\frac{\sqrt{\pi}}{\sqrt{2}}(Y_2^{-1}Y_2^{+1} - Y_2^{+1}Y_2^{-1})$	$i\frac{15}{4\sqrt{\pi}}\sin\theta_1\cos\theta_1\sin\theta_2\cos\theta_2\sin\varphi$
2	2	\parallel_2	$\frac{\sqrt{\pi}}{\sqrt{2}}(Y_2^{-2}Y_2^{+2} + Y_2^{+2}Y_2^{-2})$	$\frac{15}{16\sqrt{\pi}}\sin^2\theta_1\sin^2\theta_2\cos(2\varphi)$
2	2	\perp_2	$\frac{\sqrt{\pi}}{\sqrt{2}}(Y_2^{-2}Y_2^{+2} - Y_2^{+2}Y_2^{-2})$	$i\frac{15}{16\sqrt{\pi}}\sin^2\theta_1\sin^2\theta_2\sin(2\varphi)$

B Scalar $K\pi$ mass-dependent amplitude

The variation of the phase with $m(K\pi)$ in the nominal model used for the scalar $K\pi$ mass-dependent amplitude is taken from Ref. [17]. The modulus line-shape is parameterised

Table 7: Parameters used in the nominal model for the scalar $K\pi$ mass-dependent amplitude. The correlations among them are found to be small, the largest ones been of the order of 50%.

Parameter	Value
c_1	-0.287 ± 0.020
c_2	-0.180 ± 0.020
c_3	-0.106 ± 0.016
c_4	-0.066 ± 0.016

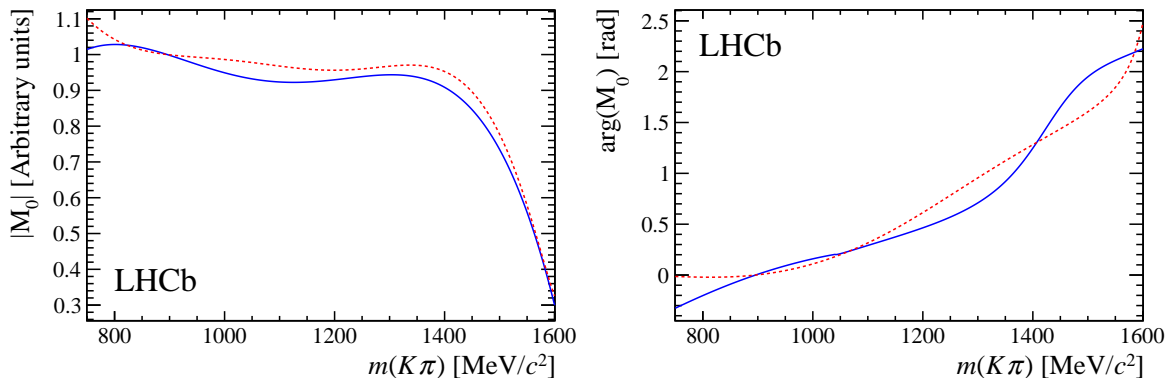


Figure 8: Line-shapes of the (left) modulus and (right) phase of the scalar $K\pi$ mass-dependent amplitude. The nominal model is shown with a solid blue line and the model-independent parameterisation, used in systematic studies, is shown with a dashed red line.

with a polynomial expansion as follows

$$|\mathcal{M}_0(m)| = 1 + \sum_{i=1}^4 c_i T_i(X(m)), \quad (20)$$

where $X(m) = (m - 1175 \text{ MeV}/c^2)/425 \text{ MeV}/c^2$, $X(m) \in [-1, 1]$, and $T_i(x)$ are the Chebyshev polynomials defined as

$$\begin{aligned} T_0(x) &= 1, & T_1(x) &= x, & T_2(x) &= 2x^2 - 1, \\ T_3(x) &= 4x^3 - 3x, & T_4(x) &= 8x^4 - 8x^2 + 1. \end{aligned} \quad (21)$$

This parameterisation is chosen to minimise parameter correlations. The values of the c_i coefficients retrieved from the decay-time-dependent fit are given in Table 7. The coefficients decrease with the order of the polynomial term. The expansion is truncated at fourth order since adding an extra term would not significantly affect the result and the size of the fifth coefficient is of the order of its statistical uncertainty. When computing systematic uncertainties, the scalar $K\pi$ mass-dependent amplitude is parameterised using a model-independent (MI) approach as follows

$$\mathcal{M}_0^{MI}(m) = \left[1 + \sum_{i=1}^4 \alpha_i T_i(X(m)) \right] + i \left[\sum_{j=0}^4 \beta_j T_j(X(m)) \right]. \quad (22)$$

The coefficients measured in the decay-time-dependent fit for this case are given in Table 8. The line-shapes of the two scalar mass amplitude models are shown in Fig. 8. Both approaches are found to be qualitatively compatible with each other.

Table 8: Coefficients used in the model-independent parameterisation of the scalar $K\pi$ mass-dependent amplitude.

Parameter	Value	Parameter	Value
α_1	-0.854 ± 0.038	β_0	0.278 ± 0.038
α_2	-0.381 ± 0.040	β_1	0.817 ± 0.079
α_3	-0.105 ± 0.032	β_2	-0.206 ± 0.082
α_4	0.046 ± 0.027	β_3	-0.367 ± 0.053
		β_4	-0.115 ± 0.040

References

- [1] R. Fleischer, *Extracting CKM phases from angular distributions of $B_{d,s}$ decays into admixtures of CP eigenstates*, Phys. Rev. **D60** (1999) 073008, arXiv:hep-ph/9903540.
- [2] R. Fleischer and M. Gronau, *Studying new physics amplitudes in charmless B_s decays*, Phys. Lett. **B660** (2008) 212, arXiv:0709.4013.
- [3] M. Ciuchini, M. Pierini, and L. Silvestrini, *$B_s^0 \rightarrow K^{(*)0}\bar{K}^{(*)0}$ CP asymmetries: Golden channels for new physics searches*, Phys. Rev. Lett. **100** (2008) 031802, arXiv:hep-ph/0703137.
- [4] S. Descotes-Genon, J. Matias, and J. Virto, *Penguin-mediated $B_{d,s} \rightarrow VV$ decays and the $B_s^0 - \bar{B}_s^0$ mixing angle*, Phys. Rev. **D76** (2007) 074005, Erratum ibid. **D84** (2011) 039901, arXiv:0705.0477.
- [5] S. Descotes-Genon, J. Matias, and J. Virto, *Analysis of $B_{d,s}$ mixing angles in presence of new physics and an update of $B_s \rightarrow K^{0*}\bar{K}^{0*}$* , Phys. Rev. **D85** (2012) 034010, arXiv:1111.4882.
- [6] B. Bhattacharya, A. Datta, M. Imbeault, and D. London, *Searching for new physics with $B_s \rightarrow K^{0(*)}\bar{K}^{0(*)}$ – a reappraisal*, Phys. Lett. **B717** (2012) 403, arXiv:1203.3435.
- [7] B. Bhattacharya, A. Datta, M. Duraisamy, and D. London, *Searching for new physics with $\bar{b} \rightarrow \bar{s} B_s^0 \rightarrow V_1 V_2$ penguin decays*, Phys. Rev. **D88** (2013) 016007, arXiv:1306.1911.
- [8] Heavy Flavor Averaging Group, Y. Amhis *et al.*, *Averages of b-hadron, c-hadron, and τ -lepton properties as of summer 2016*, arXiv:1612.07233, updated results and plots available at <http://www.slac.stanford.edu/xorg/hflav/>.
- [9] LHCb collaboration, R. Aaij *et al.*, *Precision measurement of CP violation in $B_s^0 \rightarrow J/\psi K^+ K^-$ decays*, Phys. Rev. Lett. **114** (2015) 041801, arXiv:1411.3104.
- [10] ATLAS collaboration, G. Aad *et al.*, *Measurement of the CP-violating phase ϕ_s and the B_s^0 meson decay width difference with $B_s^0 \rightarrow J/\psi\phi$ decays in ATLAS*, JHEP **08** (2016) 147, arXiv:1601.03297.

- [11] CMS collaboration, V. Khachatryan *et al.*, *Measurement of the CP-violating weak phase ϕ_s and the decay width difference $\Delta\Gamma_s$ using the $B_s^0 \rightarrow J/\psi\phi(1020)$ decay channel in pp collisions at $\sqrt{s} = 8$ TeV*, Phys. Lett. **B757** (2016) 97, arXiv:1507.07527.
- [12] LHCb collaboration, R. Aaij *et al.*, *Measurement of CP violation in $B_s^0 \rightarrow \phi\phi$ decays*, Phys. Rev. **D90** (2014) 052011, arXiv:1407.2222.
- [13] LHCb collaboration, R. Aaij *et al.*, *First observation of the decay $B_s^0 \rightarrow K^{*0}\bar{K}^{*0}$* , Phys. Lett. **B709** (2012) 50, arXiv:1111.4183.
- [14] LHCb collaboration, R. Aaij *et al.*, *Measurement of CP asymmetries and polarisation fractions in $B_s^0 \rightarrow K^{*0}\bar{K}^{*0}$ decays*, JHEP **07** (2015) 166, arXiv:1503.05362.
- [15] Particle Data Group, C. Patrignani *et al.*, *Review of particle physics*, Chin. Phys. **C40** (2016) 100001.
- [16] F. Von Hippel and C. Quigg, *Centrifugal-barrier effects in resonance partial decay widths, shapes, and production amplitudes*, Phys. Rev. **D5** (1972) 624.
- [17] J. R. Pelaez and A. Rodas, *Pion-kaon scattering amplitude constrained with forward dispersion relations up to 1.6 GeV*, Phys. Rev. **D93** (2016) 074025, arXiv:1602.08404.
- [18] K. M. Watson, *Some general relations between the photoproduction and scattering of π mesons*, Phys. Rev. **95** (1954) 228.
- [19] LHCb collaboration, A. A. Alves Jr. *et al.*, *The LHCb detector at the LHC*, JINST **3** (2008) S08005.
- [20] LHCb collaboration, R. Aaij *et al.*, *LHCb detector performance*, Int. J. Mod. Phys. **A30** (2015) 1530022, arXiv:1412.6352.
- [21] V. V. Gligorov and M. Williams, *Efficient, reliable and fast high-level triggering using a bonsai boosted decision tree*, JINST **8** (2013) P02013, arXiv:1210.6861.
- [22] T. Sjöstrand, S. Mrenna, and P. Skands, *A brief introduction to PYTHIA 8.1*, Comput. Phys. Commun. **178** (2008) 852, arXiv:0710.3820.
- [23] I. Belyaev *et al.*, *Handling of the generation of primary events in Gauss, the LHCb simulation framework*, J. Phys. Conf. Ser. **331** (2011) 032047.
- [24] D. J. Lange, *The EvtGen particle decay simulation package*, Nucl. Instrum. Meth. **A462** (2001) 152.
- [25] P. Golonka and Z. Was, *PHOTOS Monte Carlo: A precision tool for QED corrections in Z and W decays*, Eur. Phys. J. **C45** (2006) 97, arXiv:hep-ph/0506026.
- [26] Geant4 collaboration, J. Allison *et al.*, *Geant4 developments and applications*, IEEE Trans. Nucl. Sci. **53** (2006) 270; Geant4 collaboration, S. Agostinelli *et al.*, *Geant4: A simulation toolkit*, Nucl. Instrum. Meth. **A506** (2003) 250.
- [27] M. Clemencic *et al.*, *The LHCb simulation application, Gauss: Design, evolution and experience*, J. Phys. Conf. Ser. **331** (2011) 032023.

- [28] L. Breiman, J. H. Friedman, R. A. Olshen, and C. J. Stone, *Classification and regression trees*, Wadsworth international group, Belmont, California, USA, 1984.
- [29] Y. Freund and R. E. Schapire, *A decision-theoretic generalization of on-line learning and an application to boosting*, J. Comput. Syst. Sci. **55** (1997) 119.
- [30] A. Blum, A. Kalai, and J. Langford, *Beating the hold-out: Bounds for k -fold and progressive cross-validation*, in *Proceedings of the Twelfth Annual Conference on Computational Learning Theory*, COLT '99, (New York, NY, USA), pp. 203–208, ACM, 1999. doi: 10.1145/307400.307439.
- [31] M. Pivk and F. R. Le Diberder, *sPlot: A statistical tool to unfold data distributions*, Nucl. Instrum. Meth. **A555** (2005) 356, arXiv:physics/0402083.
- [32] D. Martínez Santos and F. Dupertuis, *Mass distributions marginalized over per-event errors*, Nucl. Instrum. Meth. **A764** (2014) 150, arXiv:1312.5000.
- [33] LHCb collaboration, R. Aaij *et al.*, *Measurement of the fragmentation fraction ratio f_s/f_d and its dependence on B meson kinematics*, JHEP **04** (2013) 001, arXiv:1301.5286, f_s/f_d value updated in LHCb-CONF-2013-011.
- [34] ARGUS collaboration, *Search for hadronic $b \rightarrow u$ decays*, Phys. Lett. **B241** (1990) 278.
- [35] LHCb collaboration, R. Aaij *et al.*, *Neural-network-based same side kaon tagging algorithm calibrated with $B_s^0 \rightarrow D_s^- \pi^+$ and $B_{s2}^*(5840)^0 \rightarrow B^+ K^-$ decays*, JINST **11** (2016) P05010, arXiv:1602.07252.
- [36] LHCb collaboration, R. Aaij *et al.*, *Opposite-side flavour tagging of B mesons at the LHCb experiment*, Eur. Phys. J. **C72** (2012) 2022, arXiv:1202.4979.
- [37] LHCb collaboration, R. Aaij *et al.*, *Measurement of the \bar{B}^0-B^0 and $\bar{B}_s^0-B_s^0$ production asymmetries in pp collisions at $\sqrt{s} = 7$ TeV*, Phys. Lett. **B739** (2014) 218, arXiv:1408.0275.
- [38] T. M. Karbach, G. Raven, and M. Schiller, *Decay time integrals in neutral meson mixing and their efficient evaluation*, arXiv:1407.0748.
- [39] T. du Pree, *Search for a strange phase in beautiful oscillations*, PhD thesis, Nikhef, Amsterdam, 2010, CERN-THESIS-2010-124.
- [40] T. Skwarnicki, *A study of the radiative cascade transitions between the Upsilon-prime and Upsilon resonances*, PhD thesis, Institute of Nuclear Physics, Krakow, 1986, DESY-F31-86-02.
- [41] LHCb collaboration, R. Aaij *et al.*, *Measurement of CP violation and the B_s^0 meson decay width difference with $B_s^0 \rightarrow J/\psi K^+ K^-$ and $B_s^0 \rightarrow J/\psi \pi^+ \pi^-$ decays*, Phys. Rev. **D87** (2013) 112010, arXiv:1304.2600.
- [42] D. Martínez Santos *et al.*, *Ipanema- β : Tools and examples for HEP analysis on GPU*, arXiv:1706.01420.

- [43] A. Klöckner *et al.*, *PyCUDA and PyOpenCL: A scripting-based approach to GPU run-time code generation*, *Parallel Computing* **38** (2012) 157, [arXiv:0911.3456](https://arxiv.org/abs/0911.3456).

LHCb collaboration

R. Aaij⁴⁰, B. Adeva³⁹, M. Adinolfi⁴⁸, Z. Ajaltouni⁵, S. Akar⁵⁹, J. Albrecht¹⁰, F. Alessio⁴⁰,
 M. Alexander⁵³, A. Alfonso Alberio³⁸, S. Ali⁴³, G. Alkhazov³¹, P. Alvarez Cartelle⁵⁵,
 A.A. Alves Jr⁵⁹, S. Amato², S. Amerio²³, Y. Amhis⁷, L. An³, L. Anderlini¹⁸, G. Andreassi⁴¹,
 M. Andreotti^{17,g}, J.E. Andrews⁶⁰, R.B. Appleby⁵⁶, F. Archilli⁴³, P. d'Argent¹²,
 J. Arnau Romeu⁶, A. Artamonov³⁷, M. Artuso⁶¹, E. Aslanides⁶, M. Atzeni⁴², G. Auremma²⁶,
 M. Baalouch⁵, I. Babuschkin⁵⁶, S. Bachmann¹², J.J. Back⁵⁰, A. Badalov^{38,m}, C. Baesso⁶²,
 S. Baker⁵⁵, V. Balagura^{7,b}, W. Baldini¹⁷, A. Baranov³⁵, R.J. Barlow⁵⁶, C. Barschel⁴⁰,
 S. Barsuk⁷, W. Barter⁵⁶, F. Baryshnikov³², V. Batozskaya²⁹, V. Battista⁴¹, A. Bay⁴¹,
 L. Beaucourt⁴, J. Beddow⁵³, F. Bedeschi²⁴, I. Bediaga¹, A. Beiter⁶¹, L.J. Bel⁴³, N. Beliy⁶³,
 V. Bellee⁴¹, N. Belloli^{21,i}, K. Belous³⁷, I. Belyaev^{32,40}, E. Ben-Haim⁸, G. Bencivenni¹⁹,
 S. Benson⁴³, S. Beranek⁹, A. Berezhnoy³³, R. Bernet⁴², D. Berninghoff¹², E. Bertholet⁸,
 A. Bertolin²³, C. Betancourt⁴², F. Betti¹⁵, M.O. Bettler⁴⁰, M. van Beuzekom⁴³, I.A. Bezshyiko⁴²,
 S. Bifani⁴⁷, P. Billoir⁸, A. Birnkraut¹⁰, A. Bizzeti^{18,u}, M. Bjørn⁵⁷, T. Blake⁵⁰, F. Blanc⁴¹,
 S. Blusk⁶¹, V. Bocci²⁶, T. Boettcher⁵⁸, A. Bondar^{36,w}, N. Bondar³¹, I. Bordyuzhin³²,
 S. Borghi^{56,40}, M. Borisyak³⁵, M. Borsato³⁹, F. Bossu⁷, M. Boubdir⁹, T.J.V. Bowcock⁵⁴,
 E. Bowen⁴², C. Bozzi^{17,40}, S. Braun¹², J. Brodzicka²⁷, D. Brundu¹⁶, E. Buchanan⁴⁸, C. Burr⁵⁶,
 A. Bursche^{16,f}, J. Buytaert⁴⁰, W. Byczynski⁴⁰, S. Cadeddu¹⁶, H. Cai⁶⁴, R. Calabrese^{17,g},
 R. Calladine⁴⁷, M. Calvi^{21,i}, M. Calvo Gomez^{38,m}, A. Camboni^{38,m}, P. Campana¹⁹,
 D.H. Campora Perez⁴⁰, L. Capriotti⁵⁶, A. Carbone^{15,e}, G. Carboni^{25,j}, R. Cardinale^{20,h},
 A. Cardini¹⁶, P. Carniti^{21,i}, L. Carson⁵², K. Carvalho Akiba², G. Casse⁵⁴, L. Cassina²¹,
 M. Cattaneo⁴⁰, G. Cavallero^{20,40,h}, R. Cenci^{24,t}, D. Chamont⁷, M.G. Chapman⁴⁸, M. Charles⁸,
 Ph. Charpentier⁴⁰, G. Chatzikonstantinidis⁴⁷, M. Chefdeville⁴, S. Chen¹⁶, S.F. Cheung⁵⁷,
 S.-G. Chitic⁴⁰, V. Chobanova³⁹, M. Chrzaszcz⁴², A. Chubykin³¹, P. Ciambone¹⁹,
 X. Cid Vidal³⁹, G. Ciezarek⁴⁰, P.E.L. Clarke⁵², M. Clemencic⁴⁰, H.V. Cliff⁴⁹, J. Closier⁴⁰,
 V. Coco⁴⁰, J. Cogan⁶, E. Cogneras⁵, V. Cogoni^{16,f}, L. Cojocariu³⁰, P. Collins⁴⁰, T. Colombo⁴⁰,
 A. Comerma-Montells¹², A. Contu¹⁶, G. Coombs⁴⁰, S. Coquereau³⁸, G. Corti⁴⁰, M. Corvo^{17,g},
 C.M. Costa Sobral⁵⁰, B. Couturier⁴⁰, G.A. Cowan⁵², D.C. Craik⁵⁸, A. Crocombe⁵⁰,
 M. Cruz Torres¹, R. Currie⁵², C. D'Ambrosio⁴⁰, F. Da Cunha Marinho², C.L. Da Silva⁷³,
 E. Dall'Occo⁴³, J. Dalseno⁴⁸, A. Davis³, O. De Aguiar Francisco⁴⁰, K. De Bruyn⁴⁰,
 S. De Capua⁵⁶, M. De Cian¹², J.M. De Miranda¹, L. De Paula², M. De Serio^{14,d},
 P. De Simone¹⁹, C.T. Dean⁵³, D. Decamp⁴, L. Del Buono⁸, H.-P. Dembinski¹¹, M. Demmer¹⁰,
 A. Dendek²⁸, D. Derkach³⁵, O. Deschamps⁵, F. Dettori⁵⁴, B. Dey⁶⁵, A. Di Canto⁴⁰,
 P. Di Nezza¹⁹, H. Dijkstra⁴⁰, F. Dordei⁴⁰, M. Dorigo⁴⁰, A. Dosil Suárez³⁹, L. Douglas⁵³,
 A. Dovbnya⁴⁵, K. Dreimanis⁵⁴, L. Dufour⁴³, G. Dujany⁸, P. Durante⁴⁰, J.M. Durham⁷³,
 D. Dutta⁵⁶, R. Dzhelyadin³⁷, M. Dziewiecki¹², A. Dziurda⁴⁰, A. Dzyuba³¹, S. Easo⁵¹,
 U. Egede⁵⁵, V. Egorychev³², S. Eidelman^{36,w}, S. Eisenhardt⁵², U. Eitschberger¹⁰, R. Ekelhof¹⁰,
 L. Eklund⁵³, S. Ely⁶¹, S. Esen¹², H.M. Evans⁴⁹, T. Evans⁵⁷, A. Falabella¹⁵, N. Farley⁴⁷,
 S. Farry⁵⁴, D. Fazzini^{21,i}, L. Federici²⁵, D. Ferguson⁵², G. Fernandez³⁸, P. Fernandez Declara⁴⁰,
 A. Fernandez Prieto³⁹, F. Ferrari¹⁵, L. Ferreira Lopes⁴¹, F. Ferreira Rodrigues²,
 M. Ferro-Luzzi⁴⁰, S. Filippov³⁴, R.A. Fini¹⁴, M. Fiorini^{17,g}, M. Firlej²⁸, C. Fitzpatrick⁴¹,
 T. Fiutowski²⁸, F. Fleuret^{7,b}, M. Fontana^{16,40}, F. Fontanelli^{20,h}, R. Forty⁴⁰, V. Franco Lima⁵⁴,
 M. Frank⁴⁰, C. Frei⁴⁰, J. Fu^{22,q}, W. Funk⁴⁰, E. Furfaro^{25,j}, C. Färber⁴⁰, E. Gabriel⁵²,
 A. Gallas Torreira³⁹, D. Galli^{15,e}, S. Gallorini²³, S. Gambetta⁵², M. Gandelman², P. Gandini²²,
 Y. Gao³, L.M. Garcia Martin⁷¹, J. García Pardiñas³⁹, J. Garra Tico⁴⁹, L. Garrido³⁸,
 D. Gascon³⁸, C. Gaspar⁴⁰, L. Gavardi¹⁰, G. Gazzoni⁵, D. Gerick¹², E. Gersabeck⁵⁶,
 M. Gersabeck⁵⁶, T. Gershon⁵⁰, Ph. Ghez⁴, S. Gianì⁴¹, V. Gibson⁴⁹, O.G. Girard⁴¹,
 L. Giubega³⁰, K. Gizdov⁵², V.V. Gligorov⁸, D. Golubkov³², A. Golutvin^{55,69}, A. Gomes^{1,a},
 I.V. Gorelov³³, C. Gotti^{21,i}, E. Govorkova⁴³, J.P. Grabowski¹², R. Graciani Diaz³⁸,
 L.A. Granado Cardoso⁴⁰, E. Graugés³⁸, E. Graverini⁴², G. Graziani¹⁸, A. Grecu³⁰, R. Greim⁹,
 P. Griffith¹⁶, L. Grillo⁵⁶, L. Gruber⁴⁰, B.R. Gruber Cazon⁵⁷, O. Grünberg⁶⁷, E. Gushchin³⁴,
 Yu. Guz³⁷, T. Gys⁴⁰, C. Göbel⁶², T. Hadavizadeh⁵⁷, C. Hadjivasiliou⁵, G. Haefeli⁴¹, C. Haen⁴⁰,
 S.C. Haines⁴⁹, B. Hamilton⁶⁰, X. Han¹², T.H. Hancock⁵⁷, S. Hansmann-Menzemer¹²,
 N. Harnew⁵⁷, S.T. Harnew⁴⁸, C. Hasse⁴⁰, M. Hatch⁴⁰, J. He⁶³, M. Hecker⁵⁵, K. Heinicke¹⁰,
 A. Heister⁹, K. Hennessy⁵⁴, P. Henrard⁵, L. Henry⁷¹, E. van Herwijnen⁴⁰, M. Heß⁶⁷,
 A. Hicheur², D. Hill⁵⁷, P.H. Hopchev⁴¹, W. Hu⁶⁵, W. Huang⁶³, Z.C. Huard⁵⁹, W. Hulsbergen⁴³,

T. Humair⁵⁵, M. Hushchyn³⁵, D. Hutchcroft⁵⁴, P. Ibis¹⁰, M. Idzik²⁸, P. Ilten⁴⁷, R. Jacobsson⁴⁰,
 J. Jalocha⁵⁷, E. Jans⁴³, A. Jawahery⁶⁰, F. Jiang³, M. John⁵⁷, D. Johnson⁴⁰, C.R. Jones⁴⁹,
 C. Joram⁴⁰, B. Jost⁴⁰, N. Jurik⁵⁷, S. Kandybei⁴⁵, M. Karacson⁴⁰, J.M. Kariuki⁴⁸, S. Karodia⁵³,
 N. Kazeev³⁵, M. Kecke¹², F. Keizer⁴⁹, M. Kelsey⁶¹, M. Kenzie⁴⁹, T. Ketel⁴⁴, E. Khairullin³⁵,
 B. Khanji¹², C. Khurewathanakul⁴¹, K.E. Kim⁶¹, T. Kirn⁹, S. Klaver¹⁹, K. Klimaszewski²⁹,
 T. Klimkovich¹¹, S. Koliiev⁴⁶, M. Kolpin¹², R. Kopecna¹², P. Koppenburg⁴³, A. Kosmyntseva³²,
 S. Kotriakhova³¹, M. Kozeiha⁵, L. Kravchuk³⁴, M. Kreps⁵⁰, F. Kress⁵⁵, P. Krokovny^{36,w},
 W. Krzemien²⁹, W. Kucewicz^{27,l}, M. Kucharczyk²⁷, V. Kudryavtsev^{36,w}, A.K. Kuonen⁴¹,
 T. Kvaratskheliya^{32,40}, D. Lacarrere⁴⁰, G. Lafferty⁵⁶, A. Lai¹⁶, G. Lanfranchi¹⁹,
 C. Langenbruch⁹, T. Latham⁵⁰, C. Lazzeroni⁴⁷, R. Le Gac⁶, A. Leflat^{33,40}, J. Lefrançois⁷,
 R. Lefèvre⁵, F. Lemaitre⁴⁰, E. Lemos Cid³⁹, O. Leroy⁶, T. Lesiak²⁷, B. Leverington¹²,
 P.-R. Li⁶³, T. Li³, Y. Li⁷, Z. Li⁶¹, X. Liang⁶¹, T. Likhomanenko⁶⁸, R. Lindner⁴⁰, F. Lionetto⁴²,
 V. Lisovskyi⁷, X. Liu³, D. Loh⁵⁰, A. Loi¹⁶, I. Longstaff⁵³, J.H. Lopes², D. Lucchesi^{23,o},
 M. Lucio Martinez³⁹, H. Luo⁵², A. Lupato²³, E. Luppi^{17,g}, O. Lupton⁴⁰, A. Lusiani²⁴, X. Lyu⁶³,
 F. Machefert⁷, F. Maciuc³⁰, V. Macko⁴¹, P. Mackowiak¹⁰, S. Maddrell-Mander⁴⁸, O. Maev^{31,40},
 K. Maguire⁵⁶, D. Maisuzenko³¹, M.W. Majewski²⁸, S. Malde⁵⁷, B. Malecki²⁷, A. Malinin⁶⁸,
 T. Maltsev^{36,w}, G. Manca^{16,f}, G. Mancinelli⁶, D. Marangotto^{22,q}, J. Maratas^{5,v},
 J.F. Marchand⁴, U. Marconi¹⁵, C. Marin Benito³⁸, M. Marinangeli⁴¹, P. Marino⁴¹, J. Marks¹²,
 G. Martellotti²⁶, M. Martin⁶, M. Martinelli⁴¹, D. Martinez Santos³⁹, F. Martinez Vidal⁷¹,
 A. Massafferri¹, R. Matev⁴⁰, A. Mathad⁵⁰, Z. Mathe⁴⁰, C. Matteuzzi²¹, A. Mauri⁴²,
 E. Maurice^{7,b}, B. Maurin⁴¹, A. Mazurov⁴⁷, M. McCann^{55,40}, A. McNab⁵⁶, R. McNulty¹³,
 J.V. Mead⁵⁴, B. Meadows⁵⁹, C. Meaux⁶, F. Meier¹⁰, N. Meinert⁶⁷, D. Melnychuk²⁹, M. Merk⁴³,
 A. Merli^{22,40,q}, E. Michielin²³, D.A. Milanese⁶⁶, E. Millard⁵⁰, M.-N. Minard⁴, L. Minzoni¹⁷,
 D.S. Mitzel¹², A. Mogini⁸, J. Molina Rodriguez¹, T. Mombächer¹⁰, I.A. Monroy⁶⁶, S. Monteil⁵,
 M. Morandin²³, M.J. Morello^{24,t}, O. Morgunova⁶⁸, J. Moron²⁸, A.B. Morris⁵², R. Mountain⁶¹,
 F. Muheim⁵², M. Mulder⁴³, D. Müller⁵⁶, J. Müller¹⁰, K. Müller⁴², V. Müller¹⁰, P. Naik⁴⁸,
 T. Nakada⁴¹, R. Nandakumar⁵¹, A. Nandi⁵⁷, I. Nasteva², M. Needham⁵², N. Neri^{22,40},
 S. Neubert¹², N. Neufeld⁴⁰, M. Neuner¹², T.D. Nguyen⁴¹, C. Nguyen-Mau^{41,n}, S. Nieswand⁹,
 R. Niet¹⁰, N. Nikitin³³, T. Nikodem¹², A. Nogay⁶⁸, D.P. O’Hanlon⁵⁰, A. Oblakowska-Mucha²⁸,
 V. Obraztsov³⁷, S. Ogilvy¹⁹, R. Oldeman^{16,f}, C.J.G. Onderwater⁷², A. Ossowska²⁷,
 J.M. Otalora Goicochea², P. Owen⁴², A. Oyanguren⁷¹, P.R. Pais⁴¹, A. Palano¹⁴, M. Palutan^{19,40},
 G. Panshin⁷⁰, A. Papanestis⁵¹, M. Pappagallo⁵², L.L. Pappalardo^{17,g}, W. Parker⁶⁰, C. Parkes⁵⁶,
 G. Passaleva^{18,40}, A. Pastore^{14,d}, M. Patel⁵⁵, C. Patrignani^{15,e}, A. Pearce⁴⁰, A. Pellegrino⁴³,
 G. Penso²⁶, M. Pepe Altarelli⁴⁰, S. Perazzini⁴⁰, D. Pereima³², P. Perret⁵, L. Pescatore⁴¹,
 K. Petridis⁴⁸, A. Petrolini^{20,h}, A. Petrov⁶⁸, M. Petruzzo^{22,q}, E. Picatoste Olloqui³⁸,
 B. Pietrzyk⁴, G. Pietrzyk⁴¹, M. Pikies²⁷, D. Pinci²⁶, F. Pisani⁴⁰, A. Pistone^{20,h}, A. Piucci¹²,
 V. Placinta³⁰, S. Playfer⁵², M. Plo Casasus³⁹, F. Polci⁸, M. Poli Lener¹⁹, A. Poluektov⁵⁰,
 I. Polyakov⁶¹, E. Polcarpo², G.J. Pomery⁴⁸, S. Ponce⁴⁰, A. Popov³⁷, D. Popov^{11,40},
 S. Poslavskii³⁷, C. Potterat², E. Price⁴⁸, J. Prisciandaro³⁹, C. Prouve⁴⁸, V. Pugatch⁴⁶,
 A. Puig Navarro⁴², H. Pullen⁵⁷, G. Punzi^{24,p}, W. Qian⁵⁰, J. Qin⁶³, R. Quagliani⁸, B. Quintana⁵,
 B. Rachwal²⁸, J.H. Rademacker⁴⁸, M. Rama²⁴, M. Ramos Pernas³⁹, M.S. Rangel², I. Raniuk^{45,†},
 F. Ratnikov^{35,x}, G. Raven⁴⁴, M. Ravonel Salzgeber⁴⁰, M. Reboud⁴, F. Redi⁴¹, S. Reichert¹⁰,
 A.C. dos Reis¹, C. Remon Alepuz⁷¹, V. Renaudin⁷, S. Ricciardi⁵¹, S. Richards⁴⁸, M. Rihl⁴⁰,
 K. Rinnert⁵⁴, P. Robbe⁷, A. Robert⁸, A.B. Rodrigues⁴¹, E. Rodrigues⁵⁹,
 J.A. Rodriguez Lopez⁶⁶, A. Rogozhnikov³⁵, S. Roiser⁴⁰, A. Rollings⁵⁷, V. Romanovskiy³⁷,
 A. Romero Vidal^{39,40}, M. Rotondo¹⁹, M.S. Rudolph⁶¹, T. Ruf⁴⁰, P. Ruiz Valls⁷¹, J. Ruiz Vidal⁷¹,
 J.J. Saborido Silva³⁹, E. Sadykhov³², N. Sagidova³¹, B. Saitta^{16,f}, V. Salustino Guimaraes⁶²,
 C. Sanchez Mayordomo⁷¹, B. Sanmartin Sedes³⁹, R. Santacesaria²⁶, C. Santamarina Rios³⁹,
 M. Santimaria¹⁹, E. Santovetti^{25,j}, G. Sarpis⁵⁶, A. Sarti^{19,k}, C. Satriano^{26,s}, A. Satta²⁵,
 D.M. Saunders⁴⁸, D. Savrina^{32,33}, S. Schael⁹, M. Schellenberg¹⁰, M. Schiller⁵³, H. Schindler⁴⁰,
 M. Schmelling¹¹, T. Schmelzer¹⁰, B. Schmidt⁴⁰, O. Schneider⁴¹, A. Schopper⁴⁰, H.F. Schreiner⁵⁹,
 M. Schubiger⁴¹, M.H. Schune⁷, R. Schwemmer⁴⁰, B. Sciascia¹⁹, A. Sciubba^{26,k},
 A. Semennikov³², E.S. Sepulveda⁸, A. Sergi⁴⁷, N. Serra⁴², J. Serrano⁶, L. Sestini²³, P. Seyfert⁴⁰,
 M. Shapkin³⁷, I. Shapoval⁴⁵, Y. Shcheglov³¹, T. Shears⁵⁴, L. Shekhtman^{36,w}, V. Shevchenko⁶⁸,
 B.G. Siddi¹⁷, R. Silva Coutinho⁴², L. Silva de Oliveira², G. Simi^{23,o}, S. Simone^{14,d}, M. Sirendi⁴⁹,
 N. Skidmore⁴⁸, T. Skwarnicki⁶¹, I.T. Smith⁵², J. Smith⁴⁹, M. Smith⁵⁵, I. Soares Lavra¹,

M.D. Sokoloff⁵⁹, F.J.P. Soler⁵³, B. Souza De Paula², B. Spaan¹⁰, P. Spradlin⁵³, S. Sridharan⁴⁰, F. Stagni⁴⁰, M. Stahl¹², S. Stahl⁴⁰, P. Stefko⁴¹, S. Stefkova⁵⁵, O. Steinkamp⁴², S. Stemmle¹², O. Stenyakin³⁷, M. Stepanova³¹, H. Stevens¹⁰, S. Stone⁶¹, B. Storaci⁴², S. Stracka^{24,p}, M.E. Stramaglia⁴¹, M. Straticiu³⁰, U. Straumann⁴², S. Strokov⁷⁰, J. Sun³, L. Sun⁶⁴, K. Swientek²⁸, V. Syropoulos⁴⁴, T. Szumlak²⁸, M. Szymanski⁶³, S. T’Jampens⁴, A. Tayduganov⁶, T. Tekampe¹⁰, G. Tellarini^{17,g}, F. Teubert⁴⁰, E. Thomas⁴⁰, J. van Tilburg⁴³, M.J. Tilley⁵⁵, V. Tisserand⁵, M. Tobin⁴¹, S. Tolk⁴⁹, L. Tomassetti^{17,g}, D. Tonelli²⁴, R. Tourinho Jadallah Aoude¹, E. Tournefier⁴, M. Traill⁵³, M.T. Tran⁴¹, M. Tresch⁴², A. Trisovic⁴⁹, A. Tsaregorodtsev⁶, P. Tsopelas⁴³, A. Tully⁴⁹, N. Tuning^{43,40}, A. Ukleja²⁹, A. Usachov⁷, A. Ustyuzhanin³⁵, U. Uwer¹², C. Vacca^{16,f}, A. Vagner⁷⁰, V. Vagnoni^{15,40}, A. Valassi⁴⁰, S. Valat⁴⁰, G. Valenti¹⁵, R. Vazquez Gomez⁴⁰, P. Vazquez Regueiro³⁹, S. Vecchi¹⁷, M. van Veghel⁴³, J.J. Velthuis⁴⁸, M. Veltri^{18,r}, G. Veneziano⁵⁷, A. Venkateswaran⁶¹, T.A. Verlage⁹, M. Vernet⁵, M. Vesterinen⁵⁷, J.V. Viana Barbosa⁴⁰, D. Vieira⁶³, M. Vieites Diaz³⁹, H. Viemann⁶⁷, X. Vilasis-Cardona^{38,m}, M. Vitti⁴⁹, V. Volkov³³, A. Vollhardt⁴², B. Voneki⁴⁰, A. Vorobyev³¹, V. Vorobyev^{36,w}, C. Voß⁹, J.A. de Vries⁴³, C. Vázquez Sierra⁴³, R. Waldi⁶⁷, J. Walsh²⁴, J. Wang⁶¹, Y. Wang⁶⁵, D.R. Ward⁴⁹, H.M. Wark⁵⁴, N.K. Watson⁴⁷, D. Websdale⁵⁵, A. Weiden⁴², C. Weisser⁵⁸, M. Whitehead⁴⁰, J. Wicht⁵⁰, G. Wilkinson⁵⁷, M. Wilkinson⁶¹, M. Williams⁵⁶, M. Williams⁵⁸, T. Williams⁴⁷, F.F. Wilson^{51,40}, J. Wimberley⁶⁰, M. Winn⁷, J. Wishahi¹⁰, W. Wislicki²⁹, M. Witek²⁷, G. Wormser⁷, S.A. Wotton⁴⁹, K. Wyllie⁴⁰, Y. Xie⁶⁵, M. Xu⁶⁵, Q. Xu⁶³, Z. Xu³, Z. Xu⁴, Z. Yang³, Z. Yang⁶⁰, Y. Yao⁶¹, H. Yin⁶⁵, J. Yu⁶⁵, X. Yuan⁶¹, O. Yushchenko³⁷, K.A. Zarebski⁴⁷, M. Zavertyaev^{11,c}, L. Zhang³, Y. Zhang⁷, A. Zhelezov¹², Y. Zheng⁶³, X. Zhu³, V. Zhukov^{9,33}, J.B. Zonneveld⁵², S. Zucchelli¹⁵.¹ *Centro Brasileiro de Pesquisas Físicas (CBPF), Rio de Janeiro, Brazil*

² *Universidade Federal do Rio de Janeiro (UFRJ), Rio de Janeiro, Brazil*

³ *Center for High Energy Physics, Tsinghua University, Beijing, China*

⁴ *Univ. Grenoble Alpes, Univ. Savoie Mont Blanc, CNRS, IN2P3-LAPP, Annecy, France*

⁵ *Clermont Université, Université Blaise Pascal, CNRS/IN2P3, LPC, Clermont-Ferrand, France*

⁶ *Aix Marseille Univ, CNRS/IN2P3, CPPM, Marseille, France*

⁷ *LAL, Univ. Paris-Sud, CNRS/IN2P3, Université Paris-Saclay, Orsay, France*

⁸ *LPNHE, Université Pierre et Marie Curie, Université Paris Diderot, CNRS/IN2P3, Paris, France*

⁹ *I. Physikalisches Institut, RWTH Aachen University, Aachen, Germany*

¹⁰ *Fakultät Physik, Technische Universität Dortmund, Dortmund, Germany*

¹¹ *Max-Planck-Institut für Kernphysik (MPIK), Heidelberg, Germany*

¹² *Physikalisches Institut, Ruprecht-Karls-Universität Heidelberg, Heidelberg, Germany*

¹³ *School of Physics, University College Dublin, Dublin, Ireland*

¹⁴ *Sezione INFN di Bari, Bari, Italy*

¹⁵ *Sezione INFN di Bologna, Bologna, Italy*

¹⁶ *Sezione INFN di Cagliari, Cagliari, Italy*

¹⁷ *Università e INFN, Ferrara, Ferrara, Italy*

¹⁸ *Sezione INFN di Firenze, Firenze, Italy*

¹⁹ *Laboratori Nazionali dell’INFN di Frascati, Frascati, Italy*

²⁰ *Sezione INFN di Genova, Genova, Italy*

²¹ *Sezione INFN di Milano Bicocca, Milano, Italy*

²² *Sezione di Milano, Milano, Italy*

²³ *Sezione INFN di Padova, Padova, Italy*

²⁴ *Sezione INFN di Pisa, Pisa, Italy*

²⁵ *Sezione INFN di Roma Tor Vergata, Roma, Italy*

²⁶ *Sezione INFN di Roma La Sapienza, Roma, Italy*

²⁷ *Henryk Niewodniczanski Institute of Nuclear Physics Polish Academy of Sciences, Kraków, Poland*

²⁸ *AGH - University of Science and Technology, Faculty of Physics and Applied Computer Science, Kraków, Poland*

²⁹ *National Center for Nuclear Research (NCBJ), Warsaw, Poland*

³⁰ *Horia Hulubei National Institute of Physics and Nuclear Engineering, Bucharest-Magurele, Romania*

³¹ *Petersburg Nuclear Physics Institute (PNPI), Gatchina, Russia*

³² *Institute of Theoretical and Experimental Physics (ITEP), Moscow, Russia*

³³ *Institute of Nuclear Physics, Moscow State University (SINP MSU), Moscow, Russia*

- ³⁴*Institute for Nuclear Research of the Russian Academy of Sciences (INR RAS), Moscow, Russia*
- ³⁵*Yandex School of Data Analysis, Moscow, Russia*
- ³⁶*Budker Institute of Nuclear Physics (SB RAS), Novosibirsk, Russia*
- ³⁷*Institute for High Energy Physics (IHEP), Protvino, Russia*
- ³⁸*ICCUB, Universitat de Barcelona, Barcelona, Spain*
- ³⁹*Instituto Galego de Física de Altas Enerxías (IGFAE), Universidade de Santiago de Compostela, Santiago de Compostela, Spain*
- ⁴⁰*European Organization for Nuclear Research (CERN), Geneva, Switzerland*
- ⁴¹*Institute of Physics, Ecole Polytechnique Fédérale de Lausanne (EPFL), Lausanne, Switzerland*
- ⁴²*Physik-Institut, Universität Zürich, Zürich, Switzerland*
- ⁴³*Nikhef National Institute for Subatomic Physics, Amsterdam, The Netherlands*
- ⁴⁴*Nikhef National Institute for Subatomic Physics and VU University Amsterdam, Amsterdam, The Netherlands*
- ⁴⁵*NSC Kharkiv Institute of Physics and Technology (NSC KIPT), Kharkiv, Ukraine*
- ⁴⁶*Institute for Nuclear Research of the National Academy of Sciences (KINR), Kyiv, Ukraine*
- ⁴⁷*University of Birmingham, Birmingham, United Kingdom*
- ⁴⁸*H.H. Wills Physics Laboratory, University of Bristol, Bristol, United Kingdom*
- ⁴⁹*Cavendish Laboratory, University of Cambridge, Cambridge, United Kingdom*
- ⁵⁰*Department of Physics, University of Warwick, Coventry, United Kingdom*
- ⁵¹*STFC Rutherford Appleton Laboratory, Didcot, United Kingdom*
- ⁵²*School of Physics and Astronomy, University of Edinburgh, Edinburgh, United Kingdom*
- ⁵³*School of Physics and Astronomy, University of Glasgow, Glasgow, United Kingdom*
- ⁵⁴*Oliver Lodge Laboratory, University of Liverpool, Liverpool, United Kingdom*
- ⁵⁵*Imperial College London, London, United Kingdom*
- ⁵⁶*School of Physics and Astronomy, University of Manchester, Manchester, United Kingdom*
- ⁵⁷*Department of Physics, University of Oxford, Oxford, United Kingdom*
- ⁵⁸*Massachusetts Institute of Technology, Cambridge, MA, United States*
- ⁵⁹*University of Cincinnati, Cincinnati, OH, United States*
- ⁶⁰*University of Maryland, College Park, MD, United States*
- ⁶¹*Syracuse University, Syracuse, NY, United States*
- ⁶²*Pontifícia Universidade Católica do Rio de Janeiro (PUC-Rio), Rio de Janeiro, Brazil, associated to ²*
- ⁶³*University of Chinese Academy of Sciences, Beijing, China, associated to ³*
- ⁶⁴*School of Physics and Technology, Wuhan University, Wuhan, China, associated to ³*
- ⁶⁵*Institute of Particle Physics, Central China Normal University, Wuhan, Hubei, China, associated to ³*
- ⁶⁶*Departamento de Física, Universidad Nacional de Colombia, Bogota, Colombia, associated to ⁸*
- ⁶⁷*Institut für Physik, Universität Rostock, Rostock, Germany, associated to ¹²*
- ⁶⁸*National Research Centre Kurchatov Institute, Moscow, Russia, associated to ³²*
- ⁶⁹*National University of Science and Technology MISIS, Moscow, Russia, associated to ³²*
- ⁷⁰*National Research Tomsk Polytechnic University, Tomsk, Russia, associated to ³²*
- ⁷¹*Instituto de Física Corpuscular, Centro Mixto Universidad de Valencia - CSIC, Valencia, Spain, associated to ³⁸*
- ⁷²*Van Swinderen Institute, University of Groningen, Groningen, The Netherlands, associated to ⁴³*
- ⁷³*Los Alamos National Laboratory (LANL), Los Alamos, United States, associated to ⁶¹*

^a*Universidade Federal do Triângulo Mineiro (UFTM), Uberaba-MG, Brazil*

^b*Laboratoire Leprince-Ringuet, Palaiseau, France*

^c*P.N. Lebedev Physical Institute, Russian Academy of Science (LPI RAS), Moscow, Russia*

^d*Università di Bari, Bari, Italy*

^e*Università di Bologna, Bologna, Italy*

^f*Università di Cagliari, Cagliari, Italy*

^g*Università di Ferrara, Ferrara, Italy*

^h*Università di Genova, Genova, Italy*

ⁱ*Università di Milano Bicocca, Milano, Italy*

^j*Università di Roma Tor Vergata, Roma, Italy*

^k*Università di Roma La Sapienza, Roma, Italy*

^l*AGH - University of Science and Technology, Faculty of Computer Science, Electronics and Telecommunications, Kraków, Poland*

^m *LIFAELS, La Salle, Universitat Ramon Llull, Barcelona, Spain*

ⁿ *Hanoi University of Science, Hanoi, Vietnam*

^o *Università di Padova, Padova, Italy*

^p *Università di Pisa, Pisa, Italy*

^q *Università degli Studi di Milano, Milano, Italy*

^r *Università di Urbino, Urbino, Italy*

^s *Università della Basilicata, Potenza, Italy*

^t *Scuola Normale Superiore, Pisa, Italy*

^u *Università di Modena e Reggio Emilia, Modena, Italy*

^v *Iligan Institute of Technology (IIT), Iligan, Philippines*

^w *Novosibirsk State University, Novosibirsk, Russia*

^x *National Research University Higher School of Economics, Moscow, Russia*

[†] *Deceased*